Chapter 32
Molecular Symmetry and Dynamics
William G. Harter and Tyle C. Reimer
University of Arkansas
Fayetteville, AR 72701
10.25.19 version-18e

32.1. Dynamics and spectra of molecular rotors

Molecules are aggregates of two or more nuclei bound by at least one electron. The nuclei of most stable molecules can be imagined to be points in a more or less rigid body whose relative positions are constrained by an electronic bonding potential. This potential depends strongly upon the electronic state as described elsewhere in this volume. Most of this discussion is about stable molecules in their electronic ground state. The high symmetry molecules CF_4 and SF_6 are discussed in Sec. 32.5 and compared to C_{60} or "Buckyball" a recently discovered case of the highest 3D symmetry. Sec. 32.6 introduces molecules with highly excited or "loose" parts.

Motions that stretch or compress the bonds are called *vibrational* motions and give rise to spectral resonances in the infrared region of the spectrum. Typical fundamental vibrational quanta (ν_0) lie between *80 cm^{-1}* (the lowest $GeBr_4$ mode) and *3020 cm^{-1}* (the highest CH_4 mode). (A *1000 cm^{-1}* wave has a wavelength of *10* μm and a frequency defined by speed of light: *29.9 792 458 THz.*) Vibrational amplitudes are usually tiny since zero-point motions or vibrations involving one or two quanta ($\nu = 0, 1, 2,..$) are constrained by the steep bonding potential to less than a few percent of the bond lengths, but high overtones may lead to *dissociation*, i.e., molecular breakup.

Overall rotation of molecules in free space is unconstrained and gives rise to far-infrared or microwave pure rotational transitions or sidebands on top of vibrational spectra. Typical rotational quanta (*2B*) lie between *0.18 cm^{-1} (5.4 GHz)* for SF_6 and 10.6 cm^{-1} for CH_4. Individual molecules are free to rotate or translate as a whole while undergoing their tiny but rapid vibrations. Vibrating molecules may be thought of as tumbling collections of masses held together by 'springs' (the electronic vibrational potential or force field) and are known as *semi-rigid rotors*. The coupling of rotational and vibrational motion is called *rovibrational* coupling and includes *centrifugal* and *coriolis* coupling as introduced in 32.6 at the end of this chapter.

This discussion of molecular dynamics and spectra mainly involves molecular rotation and properties of rotationally excited molecules particularly those with high rotational quanta *J*. *(J = 10 - 200)* However, the discussion also applies to molecules in excited vibrational states and even certain cases of molecules in excited electronic states. The analysis of *vibronic* (vibrational-electronic), *rovibrational* (rotation-vibration), or *rovibronic* (all three) types of excitation are very complicated and is beyond the scope of this article [32.[1],[2],[3],[4],[5]], but these problems can also benefit from the elementary considerations to be introduced here.

32.1.1 Rigid rotors

As a first approximation, and for the purposes of discussing basic molecular dynamics and spectra, one may ignore vibrations and model stable molecules as stick-and-ball structures or *rigid rotors*. Then the Hamiltonian has just three terms.

$$H = AJ_x^2 + BJ_y^2 + CJ_z^2 \ . \tag{32.1}$$

Here $[J_x, J_y, J_z]$ are rotational angular momentum operators and the rotational constants are half the inverses of the principal moments of inertia of the body.

$$A = \frac{1}{2I_x} \ , \quad B = \frac{1}{2I_y} \ , \quad C = \frac{1}{2I_z} \tag{32.2}$$

This simple form follows if the *J*-coordinate system is assumed fixed to the rotor's body and aligned to its principal axes, an elementary body or *Eckart frame*.

Many molecules and particularly all diatomic molecules have two of the three rotational constants equal, say, $A = B$. Such rotors are called *symmetric tops*, and their Hamiltonian involves the usual total angular momentum squared $\mathbf{J \cdot J}$ with one body *z*-axial component J_z.

$$H = BJ_x^2 + BJ_y^2 + CJ_z^2 = BJ_x^2 + BJ_y^2 + BJ_z^2 + (C - B)J_z^2$$
$$= B\mathbf{J} \bullet \mathbf{J} + (C - B)J_z^2 \tag{32.3}$$

This gives a simple formula for the symmetric top rotational energy levels in terms of the quantum numbers *J* of total angular momentum and *K* of the body *z*-component.

$$E(J,K) = BJ(J + 1) + (C - B)K^2 \tag{32.4}$$

However, this eigenvalue formula may be a little too simple since it hides the structure of the eigenstates or eigenfunctions. Indeed, the full Schrodinger angular differential equation based upon Hamiltonian (32.1) is more lengthy. Note that *H* is written in a rotating *body* $\{\bar{x}, \bar{y}, \bar{z}\}$ coordinate frame moving relative to a star-fixed or *laboratory* frame $\{x,y,z\}$.

32.1.2 Molecular states inside and out

Rotor angular momentum eigenfunctions can be expressed as a continuous linear combination of rotor angular position states defined by Euler angles of lab azimuth α , polar angle β of body z-axis, and body azimuth or 'gauge twist' γ . The eigenfunctions are

$$\left| {}^{\ \ J}_{MK} \right\rangle = \frac{\sqrt{2J+1}}{8\pi^2} \int_0^{2\pi} d\alpha \int_0^\pi \sin\beta d\beta \int_0^{2\pi} d\gamma D_{MK}^{J\ *}(\alpha\beta\gamma) |\alpha\beta\gamma\rangle \ . \tag{32.5}$$

Here the rotor wave functions $D_{MK}^{J\ *}$ are just the conjugates of standard Wigner rotation matrices and row and column indices *M* and *K*, respectively, are the lab and body components of angular momentum. [32.6,7] It may surprise atomic physicists that polyatomic molecular angular momentum states have two kinds of azimuthal quantum numbers. In addition to the usual lab component of momentum *M* associated with the lab coordinate α (usually α and β are labeled ϕ and θ), there is a body component *K* associated with the Euler coordinate γ. ($-\gamma$ is the body azimuthal angle of the lab-z axis relative to the body $\bar{z}$ -axis.)

The physics of atomic or diatomic angular momentum states has no internal or 'body' structure so the *K*-quantum number is always zero. Unless one sets *K=0*, the energy formula

(32.4) blows up for a point particle because z-inertia for a point is zero and C is infinite. Also, the dimension of the angular momentum state multiplet of a given *J* is larger than the usual *(2J+1)* found in atomic or diatomic molecular physics. In polyatomic rotors the number of states for each *J* is *(2J+1)-squared* since both *M* and *K* quantum numbers range between *-J* and *J*.

Also surprising, and this is a more pleasant surprise, is that the molecular rotor wave functions contain, as a special (*K=0*) case, all the usual atomic spherical harmonics complete with correct normalization and phase.

$$\sqrt{4\pi}Y_m^\ell(\varphi\vartheta) = D_{m0}^\ell(\varphi\vartheta\cdot)^* \sqrt{2\ell+1} \qquad (32.6)$$

This is part of a powerful symmetry principle: group representations are quantum wave functions, and symmetry analysis is an extension of Fourier of plane e^{ikx} waves for cyclic C_n group translations as in Fourier's original work, but for <u>any</u> group of symmetry operations. The usual Fourier coefficients are replaced by *D* functions in rotational Fourier transforms embodied by eq. (32.5).

Molecular rotational analysis displays another important but little known aspect of symmetry analysis in general. For every group of symmetry operations like the external lab based rotations familiar to atomic physics, there is an independent dual group of internal or body-based operations. The external symmetry of the environment or laboratory is independent of the internal symmetry of the molecular body, and all the operations of one commute with all those of the other. So the molecular rotation group is written as an outer product $R(3)_{LAB} \otimes R(3)_{BODY}$ of the external and internal parts, and the degeneracy associated with this group's representations for a single *J* is $(2J+1)^2$ as mentioned above. It is a special $\otimes$-product, however, since the J-number is shared.

The inversion or parity operator *I* (*r*→ *-r*) can be defined to be the same for both lab and body frames. Including *I* in the rotational group *R(3)* gives the orthogonal group *O(3)=R(3)⊗{1,I}*. If parity is conserved (no weak neutral currents!) the fundamental molecular orthogonal group is $O(3)_{LAB} \otimes O(3)_{BODY}$.

How this symmetry breaks down and which levels split depends upon both the perturbative laboratory environment and the internal molecular structure. A *spherical top* Hamiltonian is eq. (32.1) with *A=B=C*. This has a full $O(3)_{BODY}$ (spherical) symmetry since it's just *B***J·J**. Given that the rotor is in an $O(3)_{LAB}$ laboratory (empty space) the original symmetry $O(3)_{LAB} \otimes O(3)_{BODY}$ remains intact and the $(2J+1)^2$ degeneracy is to be expected. However, a *symmetric* rotor in a lab vacuum has its internal symmetry broken down to $O(2)_{BODY}$ if *A=B≠C*, and the energies given by eq. (32.4) consist of internal quantum singlets for *K=0* and doublets ±*K* for *K≠0*. But, each of these levels still has a lab degeneracy of *(2J+1)* if $O(3)_{LAB}$ is still in effect. So the $(2J+1)^2$ level degeneracies are each split into multiplets of degeneracy *(2J+1)* and *2(2J+1)* for *K=0* and *K≠0*, respectively. The resulting levels are often labeled $\Sigma, \Pi, \Delta, \Phi, \Gamma$, ...in a somewhat inappropriate analogy with the atomic s, p, d, f, g, .. labels of Bohr model electronic orbitals.

Only by perturbing the lab environment can one reduce an $O(3)_{LAB}$ symmetry and split the *M*-degeneracies. For example, a uniform electric field would reduce the $O(3)_{LAB}$ to $O(2)_{LAB}$ and give *Stark* splittings which consist of external quantum singlets for *M=0* and *±M* doublets for *M≠0*. A uniform magnetic field would reduce the $O(3)_{LAB}$ to $R(2)_{LAB}$ and give *Zeeman* splittings into of external quantum singlets for each *M*. The analogy between atomic external field splitting and internal molecular rotational structure splitting is sometimes a useful one and will be used later.

32.1.3 Rigid asymmetric rotor eigensolutions and dynamics

The general case for the rigid rotor Hamiltonian (32.1) has three unequal principal inertia *(A≠B≠C)*. This is called the rigid *asymmetric top* Hamiltonian and provides a first approximation for modeling rotation of low symmetry molecules such as H_2O. Also, a number of properties of its eigensolutions are shared by more complicated systems. The dynamics of an asymmetric top is quite remarkable as anyone will find if they toss a tennis racquet in the air starting flat side up. The corresponding quantum behavior of such a molecule is also non-trivial.

Given the total angular momentum *J* one may construct a *(2J+1)*-dimensional matrix representation of *H* using standard matrix elements of angular momentum operators J_x, J_y, and J_z such as are given in Chapter 2. The *H* matrix connects states with *(2J+1)*-different body quantum numbers *K* , but the matrix is independent of the lab quantum numbers *M*, so there are *(2J+1)* identical *H* matrices; one for each value of the lab quantum number *M* .

A plot of the 21 eigenvalues of (32.1) for J=10 is shown in Figure 32.1. Here, the constants are set to *A=0.2* cm^{-1} and *C=0.6* while *B* is varied between *B=A*, which corresponds to a *prolate* symmetric top (an elongated cylindrical object) and *B=C*, which corresponds to an *oblate* symmetric top (a flattened cylindrical object or discus). For all *B* values in between *A* and *C* the object is asymmetric.

The left hand end *(A=B=0.2 cm⁻¹, C=0.6 cm⁻¹)* of the plot in Figure 32.1 corresponds to a *prolate* symmetric top. The symmetric-top level spectrum is given by eq. (32.4). It consists of a lowest singlet corresponding to *K=0* and an ascending quadratic ladder of doublets corresponding to *K=±1, ±2,...,±J*. The right hand end *(A=0.2 cm⁻¹, B=C=0.6 cm⁻¹)* of the plot corresponds to an *oblate* symmetric top with a descending quadratic ladder of levels, the *K=0* level is highest. Also, the internal *K*-axis of quantization switches from the body z-axis for *(A=B=0.2 cm⁻¹, C=0.6)* to the body x-axis for *(A=0.2 cm⁻¹, B=C=0.6 cm⁻¹)* . The lab *M*-degeneracy is invisible here, but exists nevertheless.

For intermediate values of *B* one has an asymmetric-top level structure and, strictly speaking, no single axis of quantization. As a result, the eigenlevel spectrum is quite different. A detailed display of asymmetric top levels for the case *(A=0.2 cm⁻¹, B=0.4 cm⁻¹, C=0.6 cm⁻¹)* is given at the bottom of Figure 32.2, and they are shown to correspond to semiclassical orbits to be

discussed shortly. This example is the most asymmetric top since parameter B is midway between symmetric top limits of $B=A$ and $B=C$.

The twenty-one $J=10$ asymmetric top levels are arranged into roughly ten *asymmetry doublets* and one singlet that resemble symmetric top levels except that doublets are split by varying amounts and the singlet is isolated from other levels in the middle of the band instead of being crowded at the top or bottom. The doublet splittings are magnified in circles drawn next to the levels, and these indicate that the splitting decreases quasi-exponentially with each doublet's distance from the central singlet.

Asymmetric doublet splitting is also called *superfine structure* and can be viewed to be the result of a dynamic tunneling process in a semiclassical model of rotation.[32.8,9,10] Such a model clarifies the classical-quantum correspondence for polyatomic rovibrational dynamics in general. It can also help to derive simple approximations for eigenvalues and eigenvectors.
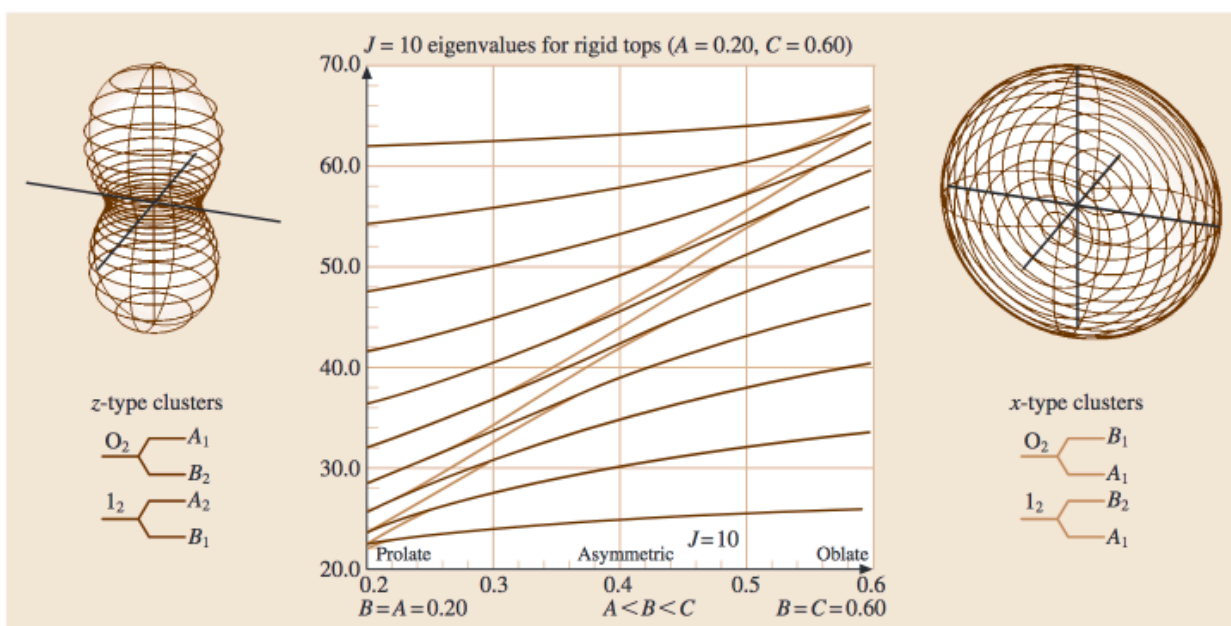

Fig. 32.1 $J = 10$ eigenvalue plot for symmetric rigid rotors. $(A = 0.2, C = 0.6 \, \text{cm}^{-1} \, A < B < C)$. Prolate and oblate RE surfaces are shown

The figures 32.1 and 32.2 contain the most elementary rotational energy surfaces (RES) that are introduced in the following section and used throughout this chapter.

J = 10

Rotation axes
near $\bar{x}$–axis

$K_2(x) \cong 9$

$\bar{J}_x$

$\bar{J}_z$

$\bar{J}_y$

Rotation axes
near $\bar{z}$–axis

$K_2(z) \cong 10$

$\bar{J}_x$

$\bar{J}_y$

...... Separatrix
region

7 8 9 $10 \cong K_2(z)$

B₁ A₂ | B₂ A₁ | B₁ A₂ | B₂ A₁

$K_2(x) \cong 10$ 9   8   7

Fine structure

5.34 cm⁻¹
=150 GHz

A₁B₁ A₂ B₂A₁

Superfine
structure

A₁ B₁ | A₂ B₂ | A₁ B₁ | A₂ B₂

8.6×
10⁻⁷cm⁻¹
= 26 kHz

7.7×
10⁻⁵ cm⁻¹
= 230 kHz

2.8×
10⁻³ cm⁻¹
= 84 MHz

5.1×
10⁻² cm⁻¹
= 1.5 GHz

$C_2(x)$-type clusters

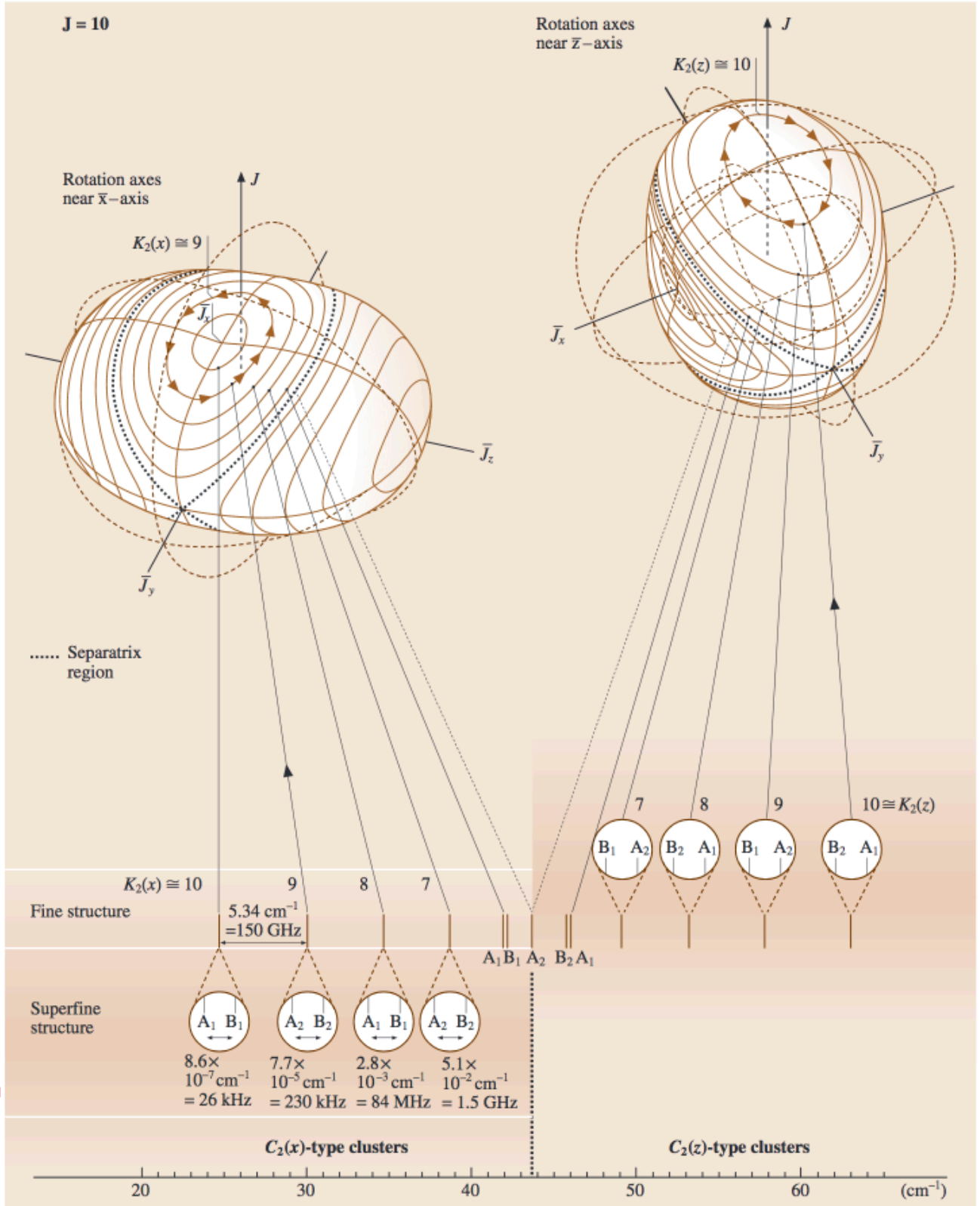$C_2(z)$-type clusters

20   30   40   50   60   (cm⁻¹)

Fig. 32.2 $J = 10$ rotational energy surface and related level spectrum for an asymmetric rigid rotator $(A = 0.2, B = 0.4, C = 0.6\,\text{cm}^{-1})$

32.2 Rotational energy surfaces and semiclassical rotational dynamics

A semiclassical model of molecular rotation can be based upon what is called a *rotational energy surface*.[32.7,8,9,10,11,12,13,14] Examples of RE surfaces for an asymmetric top are shown in the previous Figure 32.2 and for prolate and oblate symmetric tops in Figure 32.1. Each surface is a radial plot of the classical energy derived from the Hamiltonian (32.1) as a function of the polar *direction* of the classical angular momentum *J*-vector in the *body* frame. The *magnitude* |*J*| of *J* is fixed for each surface. Note, that the *J*-vector in the *lab* frame is a classical constant of the motion if there are no external perturbations. However, *J* may gyrate considerably in the moving *body* frame, but the magnitude |*J*| stays the same in all frames for free rotation.

The RE surface differs from what is called a CE or *constant energy* surface which is obtained by simply plotting *E* = *H* = *constant* in *J*-space using eq. 32.1. A rigid rotor CE surface is an ellipsoid covering a range of |*J*|-values at a single energy. An RE surface, on the other hand, is a spherical harmonic plot at a single |*J*|-value for a range of energies so it is is better for spectroscopic studies of fine structure where one value of the rotational quantum number *J* corresponds to a multiplet of energy levels or transitions. An RE surface also shows loci of high and low energy rotations. Also, it has roughly the shape of the body it represents, that is, an RES is long in directions that its molecule is long (but *vice-versa* for CES).

For a freely rotating molecule the laboratory components of the classical total angular momentum *J* are constant. If one chooses to let *J* define the lab Z-axis then the direction of the *J*-vector in the body frame is given by polar and body azimuthal coordinates β and γ, which are the second and third Euler angles, respectively. (It is conventional to use the *negatives* -β and -γ as polar coordinates but this will not be necessary here.) Then the body components of the *J*-vector are written as follows.

$$\left(J_x = |J|\sin\beta\cos\gamma, \quad J_y = |J|\sin\beta\sin\gamma, \quad J_z = |J|\cos\beta \right) \qquad (32.7)$$

Here we take the magnitude to be the quantum value $|J| = \sqrt{J(J+1)}$.

Substituting this into the Hamiltonian (32.1) gives an expression for the general rigid rotor RE surface radius in polar coordinates.

$$E(\beta,\gamma) = \langle H \rangle = J(J+1)\left(\sin^2\beta\left(A\cos^2\gamma + B\sin^2\gamma \right) + C\cos^2\beta \right) . \qquad (32.8)$$

The prolate symmetric top (*A=B<C*) expression is independent of azimuthal angle γ.

$$E(\beta) = \langle H \rangle = J(J+1)\left(B + (C-B)\cos^2\beta \right) \qquad (32.9)$$

The 3-dimensional plots of these expressions were shown in figs. 32.1 and 32.2

The RE surfaces have topography lines of constant energy (*E= constant)* that are the intersection of the RE surface (constant |*J*|) with spheres of constant energy. The topography lines are allowed classical paths of the angular momentum *J*-vector in the body frame since these paths conserve both energy and momentum.

The trajectories in the figures are special ones. They are the quantizing trajectories for total angular momentum *J=10*. For the prolate symmetric top the quantizing trajectories have

integral values for the body z-component K of angular momentum. Using a Dirac vector model, angular momentum vectors trace out a cone of altitude K and slant height $|J| = \sqrt{J(J+1)}$. Quantizing polar angles are given by

$$\Theta_K^J = \cos^{-1}\frac{K}{\sqrt{J(J+1)}} \qquad (K{=}J, J{-}1,\cdots,{-}J) \qquad (32.10)$$

These are the latitude angles of the paths on the RE surfaces in Figure 32.1 for $K=10$, 9, 8, ...,-10. (For the oblate RE surface the angles are relative to the x-axis.) If $\beta=\Theta^J{}_K$ is substituted into the symmetric top RE surface equation (32.9) the result is

$$E(\Theta_K^J) = J(J+1)B + (C - B)K^2 , \qquad (32.11)$$

which is, precisely the symmetric top eigenvalue equation (32.4). The quantizing paths are circles lying at the intersections of the Dirac angular momentum cones and the RE surface. Angle $(\Theta^J{}_K)$ is a measure of the angular momentum uncertainty ΔJ_x or ΔJ_y transverse to the z-axis of quantization. Clearly, $K=\pm J$ states have minimum uncertainty.

For the asymmetric top the classical paths which (conserve both $|J|$ and E) fall into one of two types. First there are those pairs of equal-energy orbits which go around the hills on the plus or minus end of the body z-axis and correspond to the $\pm K$ pairs of levels in the upper half of the level spectrum drawn in Figure 32.2. Then there are the pairs of levels belonging to the equal-energy orbits in either of the two valleys surrounding the body x-axis and are associated with the pairs of levels in the lower half of the level spectrum. Different eigensolutions occupy different geography.

The upper pairs of paths are seen to be distorted versions of the prolate top orbits seen on the left hand side of Figure 32.1, while the lower pairs are distorted versions of the oblate top orbits seen on the right hand side of Figure 32.1. The distortion makes J_z deviate from a constant K-value and corresponds to K-mixing in the quantum states. This also shows that one needs to consider more than one axis of quantization; the prolate-like paths are based on the z-axis, while the oblate-like paths belong to the body x-axis.

The two types of orbits, x-and-y, are separated by a so-called *separatrix* curve crossing the saddle points on either side of the body y-axis. In the example shown in Figure 32.2, the separatrix is associated with a single level that separates the upper and lower energy doublets. The doublets that are closer to the separatrix level are split more than those farther away. Apart from the splitting, the energy levels can be obtained by generalized Bohr quantization of the classical paths on the RE surface. The quantization condition is

$$\oint J_z d\gamma = K\oint J_z d\gamma = K \qquad (32.12a)$$

where

$$J_z = \sqrt{\frac{J(J+1)(C\cos^2\gamma + B\sin^2\gamma) - E}{(C\cos^2\gamma + B\sin^2\gamma) - A}} \qquad (32.12b)$$

follows from eqs. (32.7) and (32.8). The resulting E_K-values are obtained by iteration.

The doublet or superfine splitting is a quantum effect that may be associated with tunneling between orbits that would have had equal energies E_K in the purely classical or semi-classical model. Approximate tunneling rates are integrals over the saddle point between each pair of equal-energy quantizing paths. The K-th rate, or amplitude, is

$$S_K = \nu_K e^{-P_K} \qquad (32.13)$$

where ,

$$P_K = i \int_{\gamma-}^{\gamma+} d\gamma \sqrt{\frac{J(J+1)(C\cos^2\gamma + B\sin^2\gamma) - E_K}{(C\cos^2\gamma + B\sin^2\gamma) - A}} \qquad (32.14)$$

is the saddle path integral between closest approach points γ+ and γ–, and ν_K is the classical precession frequency or quantum level spacing around energy level E_K. Since there are two tunneling paths, amplitude S_K is doubled in a tunneling Hamiltonian matrix for the K-th semiclassical doublet of z and $-z = \overline{z}$ paths.

$$\langle H \rangle_K = \begin{pmatrix} E_K & 2S_K \\ 2S_K & E_K \end{pmatrix} \begin{matrix} |z\rangle \\ |\overline{z}\rangle \end{matrix} \qquad (32.15)$$

The resulting tunneling energy eigensolutions are given in Table 32.1 below.

Eigenvectors	$|z\rangle$	$|\overline{z}\rangle$	Eigenvalues
$|A\rangle$	1	1	$E^A(K) = E_K + 2S_K$
$|B\rangle$	1	−1	$E^B(K) = E_K - 2S_K$

Table 32.1 (32.15) eigensolutions

A-or B-states correspond to symmetric and anti symmetric combinations of waves localized on the two semiclassical paths. Rotational symmetry is considered below.

The total doublet splitting is $4S_K$ and decreases exponentially with the saddle point integral (32.13b). Superfine A-B splittings in Figure 32.2 range from several *GHz* near the separatrix to only 26 *kHz* for the highest-K doublets at the upper band edges.

Meanwhile the typical inter-doublet level spacing or classical *precessional* frequency is about 150 *GHz* for the $J=10$ levels shown in Figure 32.2. This K-level spacing is called *rotational fine structure* splitting, and is present in the symmetric top case, as well. (Superfine splitting of the symmetric-top doublets is exactly zero since they have $O(2)_{BODY}$ symmetry if $A=B$ or $B=C$ and tunneling amplitudes cancel.)

Classical precession of **J** in the body frame follows a "left hand rule" quite like what meteoroligists use to determine Northern Hemisphere cyclonic rotation. A left "thumbs-down" or "low" has anti-clockwise precession as does an oblate rotor valley, but a prolate RE surface "high" supports clockwise motion just like a weather "high."

Finally, consider the spacing between adjacent J-levels that is called *rotational structure* in a spectrum. This spacing is

$$E(J,K) - E(J-1,K) = 2BJ \qquad (32.16)$$

according to the symmetric top energy formulas (32.4). For this example *2BJ* is about 10 *cm⁻¹* or 300 *GHz*. It corresponds to the actual rotation frequency of the body. It is the only kind of rotational dynamics or spectra that is possible for a simple diatomic rotor. However, a diatomic

molecule may have internal electronic or nuclear spin rotation which gives additional fine structure as discussed later. [32.[1, 6, 15]]

To summarize, polyatomic molecules can be expected to exhibit all three types of rotational motion and spectra. Noted above were three types of motion (from faster to slower): *rotational*, *precessional*, and precessional *tunneling*. These were related to three kinds of spectral structure (from coarser to finer spectra): *rotational* structure, *fine* structure, and *superfine* structure, respectively. Again, this neglects internal rotational and spin effects which can have abnormally strong rotational resonance coupling due to the superfine structure. [32.[9, 16]] Examples of this are discussed further along in this chapter.

32.3 Symmetry of molecular rotors

Molecular rotational symmetry is most easily introduced using examples of rigid rotors. Molecular rotor structures may have more or less internal molecular symmetry depending on how their nuclei are positioned relative to one another in the body frame. A molecule's rotational symmetry is described by one of the elementary rotational point symmetry groups. These are the *n*-fold axial cyclic groups C_n and polygonal dihedral groups D_n (*n = 1, 2,...*), the tetrahedral group *T*, the cubic-octahedral group *O*, or the icosahedral group *Y*. All other point groups such as C_{nv} , T_d, and O_h are one of these in combination with the inversion operation *I* ($\mathbf{r} \rightarrow \text{-}\mathbf{r}$). Each of these groups consist of operations that leave at least one point (origin) of a structure fixed while mapping identical atoms or nuclei into each other in such a way that the structure ends up looking the same as it did before the operation. The point groups map onto subgroups of the nuclear permutation groups.[32.[17]]

In other words, molecular symmetry is based upon one of the most fundamental (and mysterious!) properties of atomic physics: the absolute identity of all atoms or, more precisely, nuclei of a given atomic number Z and mass number A. It is the identity of the so called 'elementary' electronic and nucleonic constituent particles that underlies the symmetry.

A quite mysterious axiom of modern physics is the Pauli principle that states: *All half-integer spin particles are antisymmetrized with every other one of their kind in the universe*. The Pauli-Fermi antisymmetry and related Bose-Einstein symmetrization principle determine much of molecular symmetry and dynamics just as the Pauli exclusion principle is fundamental to atomic and molecular electronic structure.

C_2	1	R
A	1	1
B	1	−1

Table 32.2 Character table for symmetry group C_2

Table 32.3 Character table for symmetry group D_2

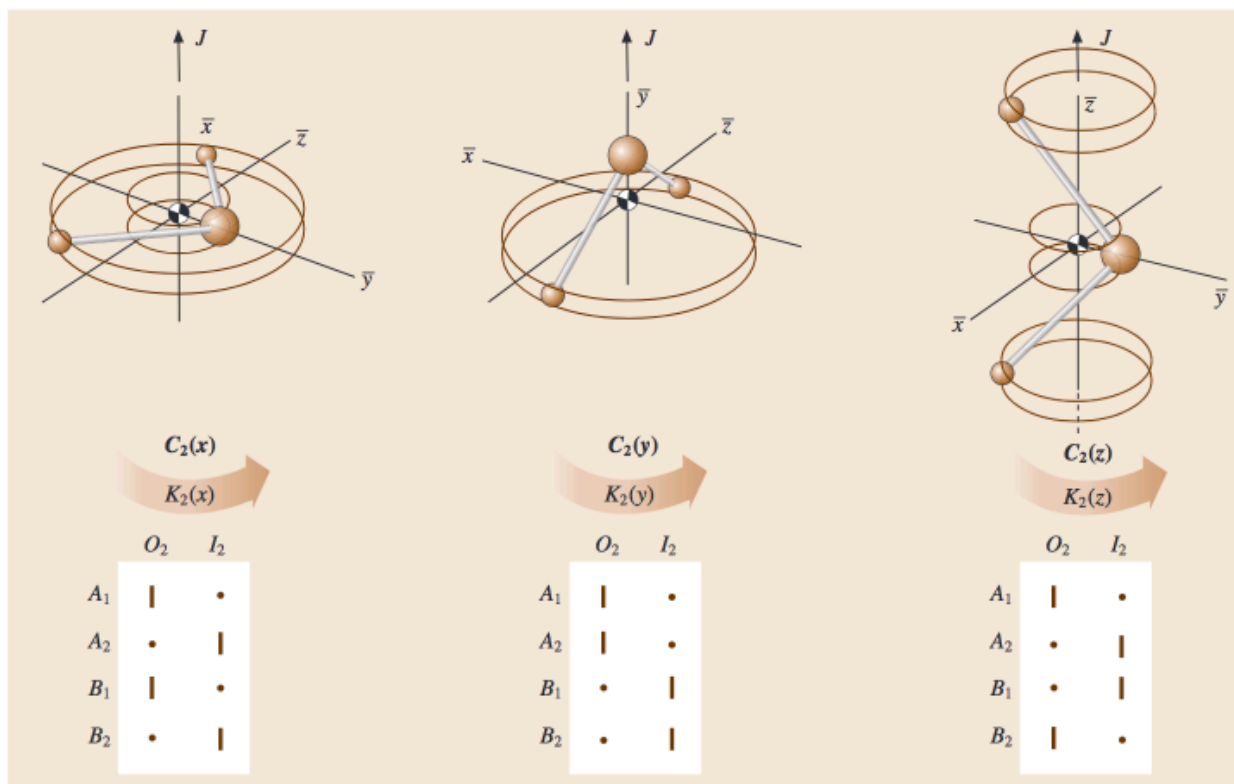| D_2	1	R_x	R_y	R_z
A_1	1	1	1	1
A_2	1	−1	1	−1
B_1	1	1	−1	−1
B_2	1	−1	−1	1

Fig. 32.3 Tables of correlations between D_2 symmetry species and the even (0_2) and odd (I_2) symmetric species of subgroups $C_2(x)$, $C_2(y)$, and $C_2(z)$

32.3.1 *Asymmetric rotor symmetry analysis*

For an asymmetric rigid rotor, any rotation that interchanges x, y, or z-axes of the body cannot possibly be a symmetry since all three axes are assumed to have differing inertial constants. This restricts one to consider only 180° rotations about the body axes, and these are the elements of the rotor groups C_2 and D_2.

The two symmetry types for C_2 are *even* (denoted A or 0_2) and *odd* (denoted B or 1_2) with respect to a 180° rotation. For D_2 which is just $C_2 \otimes C_2$, the four symmetry types are *even-even* (denoted A_1), *even-odd* (denoted A_2), *odd-even* (denoted B_1), and *odd-odd* (denoted B_2) with respect to 180° rotations about y and x-axes, respectively. (The z-symmetry is determined by a product of the other two since $\mathbf{R}_z = \mathbf{R}_x \mathbf{R}_y$.) This is summarized by the character Table 32.2 and Table 32.3.

C_2	1	R
A	1	1
B	1	−1

Table 32.2

D_2	1	$\mathbf{R}_x$	$\mathbf{R}_y$	$\mathbf{R}_z$
A_1	1	1	1	1
A_2	1	-1	1	-1
B_1	1	1	-1	-1
B_2	1	-1	-1	1

Table 32.3

The rotational energy surface for a rigid rotor shown in Figure 32.2 is invariant to 180° rotations about each of the three body axes. Therefore its Hamiltonian symmetry is D_2 and its quantum eigenlevels must correspond to one of the four types listed under D_2 in table 32.3. The D_2 symmetry labels are called *rotational* (or in general *rovibronic*) *species* of the molecular state. The species label the symmetry of a quantum wave function associated with a pair of C_2 symmetric semiclassical paths.

The classical *J*-paths come in D_2 symmetric pairs, but each individual classical *J*-path on the rigid rotor RE surface has a C_2 symmetry that is a subgroup of D_2. Each path in the valley around the x-axis is invariant to just the 180° rotation around the x-axis. This is C_2 *(x)* symmetry. The other member of its pair that goes around the negative x-axis also has this local C_2 *(x)* symmetry. The combined pair of paths has the full D_2 symmetry but classical mechanics does not permit occupation of two separate paths. Such co-occupation is a completely quantum effect.

Similarly, each individual *J*-path on the hill around the z-axis is invariant to just the 180° rotation around the z-axis and so it has C_2 *(z)* symmetry as does the equivalent path around the negative z-axis. Only the separatrix has the full D_2 symmetry since its pairs are linked up on the y-axis to form the boundary between x and z paths. No *J*-paths encircle the unstable y-axis since it is a saddle point.

Each classical *J*-path near x or z axes belongs to a particular *K*-value through semiclassical quantization conditions (32.12). Depending upon whether the *K*-value is *even* (denoted by 0_2) or odd (denoted by 1_2) the corresponding *K*-doublet will be correlated with a pair of D_2 species as shown in the columns of correlation tables in Figure 32.3. These three correlation tables give the axial 180° rotational symmetry of each D_2 species for rotation near

each body axis x, y and z, respectively, but only the stable rotation axes x and z support stable path doublets for this Hamiltonian (32.1).

For example, consider $K=10$ paths which lie lowest in the x-axis valleys. Since $K=10$ is even (0_2) it is correlated with an A_1 and B_1 superfine doublet (see the 0_2 column of the C_2 (x) table). On the high end near the z-axis hill top $K=10$ gives rise to an A_1 and B_2 doublet (see the 0_2 column of the C_2 (z) table). All the doublets in Figure 32.2 may be assigned in this way.

32.4 Tetrahedral-octahedral rotational dynamics and spectra

The highest symmetry rigid rotor is the *spherical top* for which the three inertial constants are equal $(A=B=C)$. As previously mentioned the spherical top Hamiltonian

$$H = B\mathbf{J} \bullet \mathbf{J}$$

has full $R(3)_{LAB} \otimes R(3)_{BODY}$ symmetry. Inversion parity symmetry is $O(3)_{LAB} \otimes O(3)_{BODY}$. In any case the J-levels are $(2J+1)^2$-fold degenerate. The resulting $BJ(J+1)$ energy expression is the first approximation for molecules which have regular polyhedral symmetry of, for example, a tetrahedron (CF_4), cube (C_6H_6), octahedron (SF_6), dodecahedron or icosahedron ($C_{20}H_{20}$, $B_{12}H_{12}$, or C_{60} [32.24-25] discussed in later sections.). Rigid regular polyhedra have isotropic or equal inertial constants and rotate just like they were perfectly spherical distributions of mass.

No molecule can really have spherical $O(3)_{BODY}$ symmetry since even the highest symmetry molecules are made of a finite number of nuclear mass points. Evidence of octahedral or tetrahedral symmetry shows up in fine structure splittings analogous to those for asymmetric tops. However, spherical top fine structure is due to symmetry breaking caused by anisotropic or tensor rotational distortion, and so they are called *semi-rigid* rotors.

32.4.1 Semi-rigid octahedral rotors and centrifugal tensor Hamiltonians

The lowest order tensor centrifugal distortion perturbation has the same form for both tetrahedral and octahedral molecules. It is simply a sum of fourth powers of angular momentum operators given in the third term below. The first two terms are scalar rotor energy (32.16) and scalar centrifugal energy.

$$H = B|J|^2 + D|J|^4 + 10t_{044}\left(J_x^4 + J_y^4 + J_z^4 - (3/5)J^4\right) \qquad (32.16)$$

The tensor term includes the scalar $(3/5)J^4$ to preserve the center of gravity of the tensor level splitting. Hecht [32.18] first used this type of semi-rigid rotor Hamiltonian in the study of methane (CH_4) spectra.

The scalar terms do not reduce the symmetry or split the levels, but the tensor (t_{044}) term breaks the molecular symmetry from $O(3)_{LAB} \otimes O(3)_{BODY}$ to a lower symmetry subgroup $O(3)_{LAB} \otimes T_{d\ BODY}$ or $O(3)_{LAB} \otimes O_{h\ BODY}$ and splits the $(2J+1)^2$-fold degeneracy into intricate fine structure patterns which are analogous to cubic crystal field splitting of atomic orbitals. The first calculations of tensor spectra were done by direct numerical diagonalization.[32.18,19,20,21] As a result many subtle symmetry properties were missed. Semiclassical analyses [32.22] described in the following Sections exposes these properties.

32.4.2 Octahedral and tetrahedral rotational energy surfaces

By substituting eq. (32.7) and plotting the energy as a function of body polar angles β and γ one obtains a rotational energy (RE) surface, two views of which are shown in Figure 32.4. Here the tensor term is exaggerated in order to exhibit the topography clearly. (In *(n=0)* SF_6 the t_{044} coefficient is only about *5.44 Hz* while the rotational constant is $B=0.09\ cm^{-1}$. The t_{244} coefficient of *(n=1)* SF_6 is much greater.)

A positive tensor coefficient $(t_{044}>0)$ gives an octahedral shaped RE surface shown in Figure 32.4. This is appropriate for octahedral molecules since they are least susceptible to distortion by rotations around the x, y, and z-axes that are the strong radial bonds. Thus rotational energy is highest for a *J*-vector near one of six body axes *(±1,0,0)*, *(0,±1,0)*, or *(0,0,±1)*, that is, one of six RE surface hills in Figure 32.4.

However, if the *J*-vector is set in any of the eight inter-axial directions *(±1,±1,±1)* the centrifugal force will more easily bend the weaker angular bonds, raise the molecular inertia, and lower the rotational energy to that of one of the eight valleys on the RE surface in Figure 32.4.

A negative tensor coefficient $(t_{044}<0)$ gives a cubic shaped RE surface. Usually this is appropriate for cubic and tetrahedral molecules since they are most susceptible to distortion by rotations around the x, y, and z-axes that lie between the strong radial bonds on the cubic diagonals. Instead of six hills and eight valleys one finds six valleys and eight hills on the cubic RE surface. Both freon CF_4 and cubane C_8H_8 are like that.

It should be noted that a semi-rigid tetrahedral rotor may have the same form of rotational Hamiltonian and RE surface as a cubic rotor. The four tetrahedral atomic sites are in the same directions as four of the eight cubic sites. The other four cubic sites form an inverted tetrahedron of the same shape.

If only tetrahedral symmetry was required, the Hamiltonian might have third order terms like $J_x J_y J_z$. However, such terms do not have time-reversal symmetry that makes energy the same for *J* and *-J* or rotational sense would matter. So simple rotor RE surfaces have inversion symmetry even if their molecules do not. Compound rotors containing spins or other rotors may have "lopsided" pairs of RES as shown in Sec. 32.6.

32.4.3 Octahedral and tetrahedral rotational fine structure

An example of rotational fine structure for angular momentum quantum number *J=30* is shown in Figure 32.4. The levels consist mainly of clusters of levels belonging to the octahedral symmetry species A_1, A_2, E, T_1, or T_2. The characters of these species are the following Table 32.4. (The tetrahedral T_d group has a similar table where T_1 and T_2 are often labeled F_1 and F_2).

O	0°	120°	180°	90°	180°
A_1	1	1	1	1	1
A_2	1	1	1	−1	−1
E	2	−1	2	0	0
T_1	3	0	−1	1	−1
T_2	3	0	−1	−1	1

Table 32.4 O-group characters

The first column gives the dimension or degeneracy of each species; A_1, A_2, are singlets, E is a doublet, while T_1 and T_2 are triplets. These species form two clusters (A_1, T_1, T_2, A_2) and (T_2, E, T_1) on the low end of the spectrum and six clusters (T_1, T_2), (A_2, T_2, E), (T_1, T_2), (E, T_1, A_1), (T_1, T_2), and (A_2, T_2, E) on the upper part of the spectrum. (See the right hand side of Figure 32.4.) Note that the total dimension or (near) degeneracy for each of the two lower clusters is eight: $(1+3+3+1)$ and $(3+2+3)$, while the upper clusters each have a six-fold (near) degeneracy: $(3+3)$, $(1+3+2)$, ...etc.

Each of the two lower eight-fold clusters can be associated with a semiclassical quantizing paths in an RE surface valley as shown in Figure 32.4. The eight-fold dimension or (near) degeneracy occurs because each quantizing path is repeated eight times; once in each of eight identical valleys. Similarly, the six-fold cluster dimension $((3+3), (1+3+2), ...$etc.$)$ occurs because there are six identical hills and each quantizing path is repeated six times around the surface.

The majority of the paths lie on the hills because the hills are bigger than the valleys. The hills subtend a half angle of 35.3° to the separatrix, while the valleys only have 19.5°. To estimate the number of paths or clusters in hills or valleys one may calculate the angular momentum cone angles for $J=30$ using eq. (32.10). The results are displayed in Figure 32.5. The result is consistent with the spectrum in Figure 32.4. Only the two highest K-values of $K=30$ and 29 have cones small enough to fit in the valleys, while the six states of $K=30, 29, 28, 27, 26,$ and 25 can fit onto the hills.

The angular momentum cone formula also provides an estimate for each level cluster energy. The estimates become more precise as K increases (approaching J) so the uncertainty angle decreases. Higher-K paths are more nearly circular and therefore more nearly correspond to symmetric top quantum states of pure K. The paths on octahedral RE surfaces are more nearly circular for a given K than are those on the asymmetric top RE surface, and so one can better approximate octahedral rotor states with those of a symmetric top.
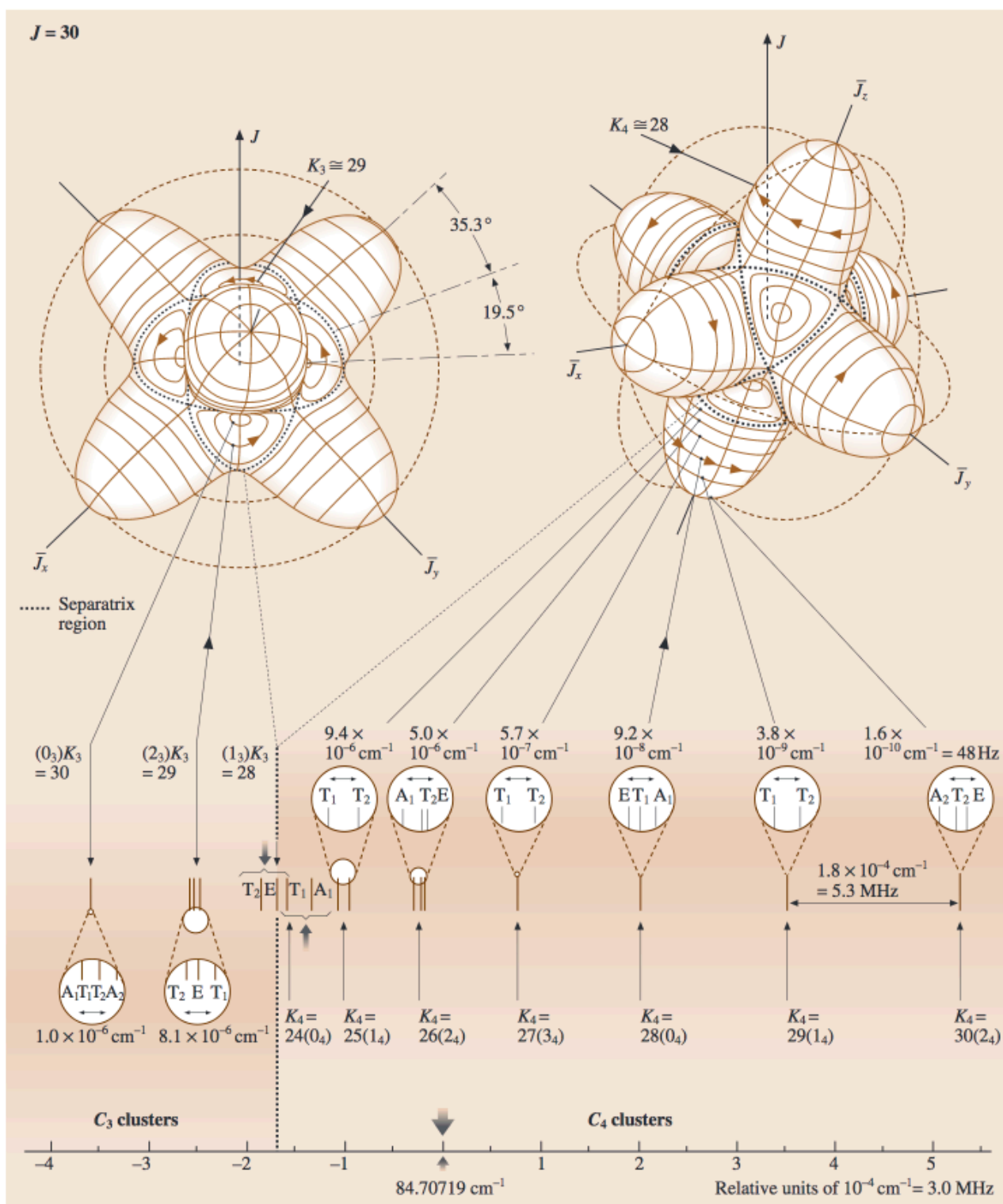
Fig. 32.4 $J = 10$ rotational energy surface related level spectrum for a semirigid octahedral or thetrahedral rotor

32.4.4 Octahedral superfine structure

The octahedral RE surface has many more local hills and valleys and corresponding types of semiclassical paths than one finds on the rigid asymmetric top RE surface. The tunneling between multiple paths gives an octahedral superfine structure that is more complicated than the asymmetric top doublets. Still the same symmetry correlations and tunneling mechanics apply.

First, the octahedral symmetry must be correlated with the local symmetry of the paths on the hills and in the valleys. The hill paths have a C_4 symmetry while the valley paths have a local C_3 symmetry. This is seen most clearly for the low-K paths near the separatrix that are less circular. The C_3 and C_4 correlations are given in Figure 32.6 with corresponding sketches of molecular rotation for each type of path.

To find the octahedral species associated with a $K_3=30$ path in a C_3 valley one notes that 30 is 0 modulo 3. Hence the desired species are found in the 0_3 column of the C_3 correlation table. One finds (A_1, A_2, T_1, T_2) and this is what appears (not necessarily in that order) on the extreme lower left hand side of Figure 32.4. Similarly, the species (A_2, E, T_2) for a $K_4=30$ path on top of a C_4 hill are found in the 2_4 column of the C_4 correlation table since 30 is 2 modulo 4, and these appear on the other side of Figure 32.4. Similarly, clusters (T_1, T_2) for $K_4=29$, and (A_1,E,T_1) for $K_4=28$ follow.

A multiple-path tunneling calculation analogous to the one for rigid rotors can be applied to approximate octahedral superfine splittings. Consider the cluster (A_1,E,T_1) for $K_4=28$ for example. One may label six C_4-symmetric paths located on octahedral vertices on opposite sides of $\pm x$, $\pm y$, and $\pm z$-axes as on the righthand side of matrix H in (32.17) that is the tunneling matrix between the six paths.

$$\langle H \rangle_{K_4=28} = \begin{pmatrix} H & 0 & S & S & S & S \\ 0 & H & S & S & S & S \\ S & S & H & 0 & S & S \\ S & S & 0 & H & S & S \\ S & S & S & S & H & 0 \\ S & S & S & S & 0 & H \end{pmatrix} \begin{matrix} |x\rangle \\ |\bar{x}\rangle \\ |y\rangle \\ |\bar{y}\rangle \\ |z\rangle \\ |\bar{z}\rangle \end{matrix} \qquad (32.17)$$

Here the tunneling amplitude S is assumed between nearest neighbor octahedral vertices but is assumed to be zero between antipodal vertices. The eigenvectors and eigenvalues for this matrix are given in the Table 32.5. K-cone polar uncertainty angles for J=30 are listed in Fig. 32.5.

Angular momentum cones for J = 30

$\Theta = 10.3°$ $K = 30$
$\Theta = 18.0°$ $K = 29$ 3-fold cutoff 19.5°
$\Theta = 23.3°$ $K = 28$
$\Theta = 27.7°$ $K = 27$
$\Theta = 31.5°$ $K = 26$
$\Theta = 34.9°$ $K = 25$ 4-fold cutoff 35.3°
$\Theta = 38.1°$ $K = 24$

30

$\sqrt{30(31)}$
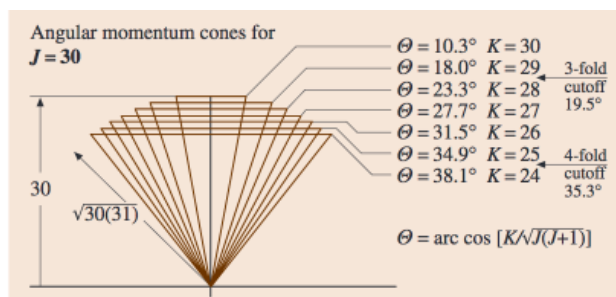
$\Theta = \text{arc cos}\ [K/\sqrt{J(J+1)}]$

Fig. 32.5 $J = 30$ angular momentum cone half angles and octahedral cutoffs

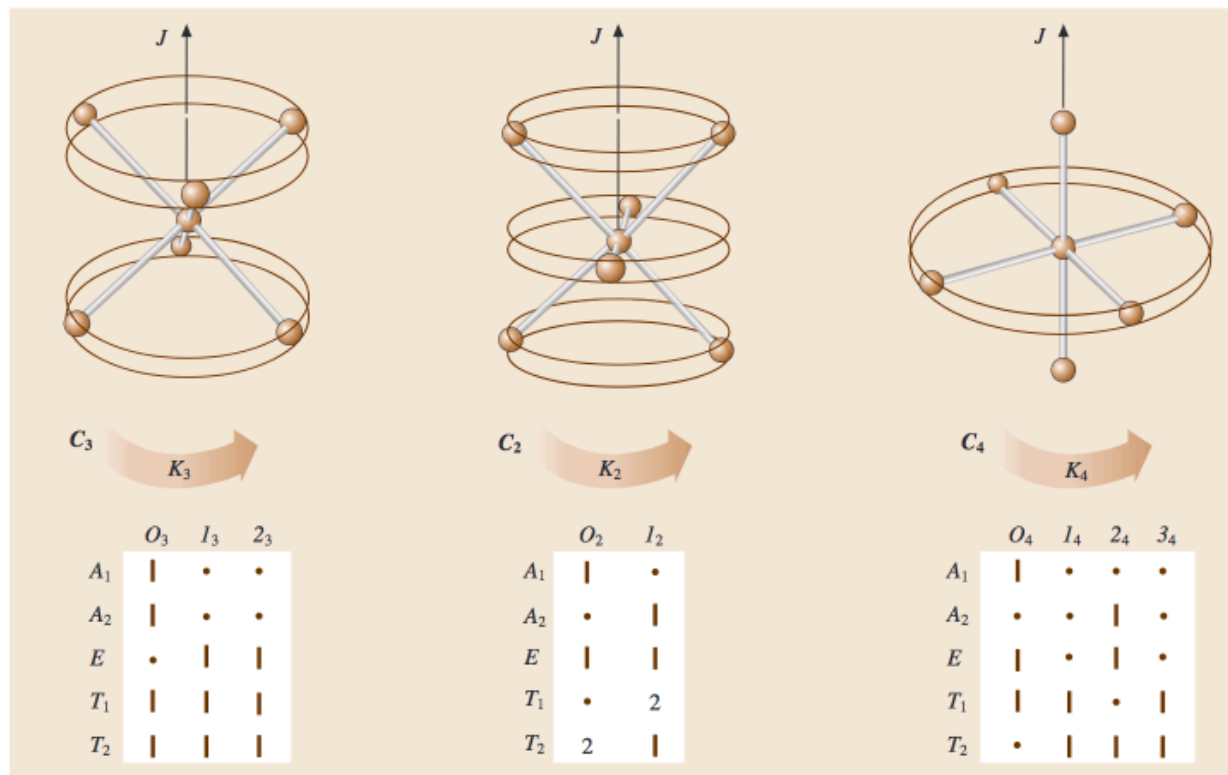Editorial Note 2: The bars (I) in three Fig. 32.6 tables should be "ones" (1)

Fig. 32.6 Tables of correlations between 0 symmetry species and the cyclic axial symmetry species (K_p means K mod p) of subgroups C_3, C_2 and C_4

Eigenvector	$\|x\rangle$	$\|\bar{x}\rangle$	$\|y\rangle$	$\|\bar{y}\rangle$	$\|z\rangle$	$\|\bar{z}\rangle$	Eigenvalue
$\sqrt{6}\|A_1\rangle =$	1	1	1	1	1	1	$E^{A_1} = H + 4S$
$\sqrt{12}\|E,1\rangle =$	2	2	−1	−1	−1	−1	$E^E = H - 2S$
$2\|E,2\rangle =$	0	0	1	1	−1	−1	
$\sqrt{2}\|T_1,1\rangle =$	1	−1	0	0	0	0	$E^{T_1} = H$
$\sqrt{2}\|T_1,2\rangle =$	0	0	1	−1	0	0	
$\sqrt{2}\|T_1,3\rangle =$	0	0	0	0	1	−1	

Table 32.5 $H_{K=28}$ matrix solutions

This predicts that the triplet (T_1) level should fall between the singlet (A_1) and the doublet (E) levels and the singlet-triplet spacing ($4S$) should be twice the splitting ($-2S$) between triplet and doublet. This 2:1 ratio is observed in (E, T_1, A_1) and (A_2, T_2, E) clusters that can be resolved and in numerical calculation, as well. [32.18-21]

The tunneling amplitudes can be calculated by a separatrix path integral analogous to the asymmetric top formula (32.13).[32.10, 11] As shown in Figure 32.4, the tunneling rates or superfine splittings near the separatrix are ~1 MHz which is only slightly slower than the classical precessional frequency. But as K approaches J on the hilltops, the tunneling rate slows quasi-exponentially to ~3 mHz, that is by a factor of about 10^{-9}.

32.5 High resolution rovibrational structure

A display of spectral hierarchy for higher and higher resolution is shown in Figure 32.7 for the *630 cm^{-1}* or *16μm* bands of CF$_4$[32.[22],[23],[24],[25]] This summarizes the possible rovibrational spectral structures and place them in a larger context. The ν$_4$ resonance in part (a) corresponds to a dipole active n$_4$=0→1 vibrational transition and is just one of many vibrational structures to study. The *P(54)* sideband resonance in part (b) corresponds to a (J=54)→(J-1) rotational transition and is just one of hundreds of rotational structures within the ν$_4$ bands.

Each band is like a Russian doll; it contains structure within structure within structure down to the resolution of few tens of Hertz. Examples of rotational fine and superfine structures described in Sections 32.4 are shown in Fig. 32.7c-d, but even more resolution is needed to see the hyperfine structure in Fig. 32.7e. [32.[26]] Such extreme resolution was reached with a CO$_2$ saturation absorption spectrometer. [32.[27],[28]] The 10μm bands of SF$_6$ and SiF$_4$ have been studied in this manner, the latter being similar to CF$_4$.

32.5.1 Tetrahedral nuclear hyperfine structure

High resolution spectral studies of SiF$_4$ showed unanticipated effects involving the four fluorine nuclear spin and magnetic moments and their associated hyperfine states. First, and this was well known, the Pauli principle restricts the nuclear spin multiplicity associated with each of the rotational symmetry species in much the same way that atomic *L-S* coupled states ^{2S+1}L have certain spin multiplicities (*2S+1*) allowed for a given orbital *L* species involving two or more equivalent electrons. Secondly, and this was not so well known, since superfine splittings can easily be tiny, different spin species can end up close enough that hyperfine interactions, however small, can cause strongly resonant mixing of the normally inviolate species. Finally, one gets to witness a pure and simple form of spontaneous symmetry breaking in which otherwise equivalent nuclei fall into different subsets due to quantum rotor dynamics.

Connecting nuclear spin to rotational species is done by correlating the full permutation symmetry (*S$_n$* for XY$_n$ molecules) with the full molecular rotation and parity symmetry (*O(3)$_{LAB}$⊗T$_d$ $_{BODY}$* for CF$_4$ molecules or *O(3)$_{LAB}$⊗O$_h$ $_{BODY}$* and for SF$_6$). For four spin-^{1}/$_2$ nuclei, the Pauli principle allows a total spin of *I=2* having multiplicity of five (*2I+1=5*) for (*J$^+$, A$_2$*) or (*J$^-$, A$_1$*) species, but excludes (*J$^-$, A$_2$*) or (*J$^+$, A$_1$*) species altogether. Pauli allowed spin for (*J$^+$, T$_1$*) or (*J$^-$, T$_2$*) species is *I=1* with a multiplicity of three, but there are no allowed (*J$^+$, T$_2$*) or (*J$^-$, T$_1$*) species. Finally, both (*J$^+$, E*) and (*J$^-$, E*) belong to singlet spin *I=0* and are singlet partners to an *inversion doublet*. (None of the other species can have both + and - parity.)

The *E* inversion doublet is analogous to the doublet in NH$_3$ that is responsible for the ammonia maser. However, NH$_3$ inversion is not feasible in CF$_4$ or SiF$_4$ and so the splitting of the *E* doublet in these molecules is due to hyperfine resonance. [32.[26]] and analyzed by unitary symmetry [32.[9],[16]] given below and in later sections.

Fig. 32.7a–e Rovibrational structure in the 630 cm^{-1} or 16 µm bands of CF$_4$ [32.16]. (**a**) Vibrational resonances and band profiles. (Raman spectra from [32.23]). (**b**) Rotational P, Q, and R band structur corresponding to $J \rightarrow J-1$, $J \rightarrow J+1$ transitions. (FTIR spectra from [32.24]). (**c**) P(54) rotational fine structure due to rotation–vibration coupling and angular momentum precessional motion. (Laser diode spectra from [32.25]). (**d**) Superfine structure due to precessional tunneling [32.26]. (**e**) Hyperfine structure due to nuclear spin precession [32.26]

    The Pauli analysis gives the number of hyperfine lines that each species would exhibit if it was isolated and resolved as shown in the center of Figure 32.7(e). The rotational singlets A_1 and A_2 give five lines each, the rotational triplets T_1 and T_2 are spin triplets, and the rotational doublet E is a spin singlet but an inversion doublet. If the hyperfine structure of a given species A_1, A_2, T_1, T_2, or E is not resolved then their line heights are proportional to their total spin weights of $5, 5, 3, 3,$ and 2, respectively.

    If the unresolved species are clustered then the total spin weights of each will add to give characteristic cluster line height. The line heights of the C_4 clusters $(T_1, T_2), (A_2, T_2, E), (T_1, T_2),$ (E, T_1, A_1) are $6, 10, 6, 10$, respectively. The line heights of the C_3 clusters (A_1, T_1, T_2, A_2), $(T_1,$ $E, T_2)$, (T_1, E, T_2) are $16, 8, 8$, respectively. This is roughly what is seen in the $P(54)$ spectrum in Figure 32.7 (c).

32.5.2 Superhyperfine structure and spontaneous symmetry breaking

Superfine cluster splittings ($2S$, $4S$, etc.) are proportional to the J-precessional tunneling or 'tumbling' rates between equivalent C_3 or C_4 symmetry axes that decrease with increasing K_3 or K_4. At some point the superfine splittings decrease to less than the hyperfine splittings. (That are meanwhile actually increasing with K.) The resulting collision of superfine and hyperfine structure has been called *superhyperfine* structure or *Case 2* clusters. The following is a rough sketch of the phenomenology of this quite complex spectra using the results of Pfister [32.26].

As long as the tunneling rates are a megahertz or more the nuclear spins will tend to average over spherical top motion. The spins couple into states of good total nuclear spin I that in turn couple weakly with the overall angular momentum and with well defined rovibrational species A_1 , A_2 , T_1 , T_2 , or E as described above. The resulting coupling is called *Case 1*. It is analogous to LS-coupling in atoms.

Stick figures for two examples of spectra observed by Pfister [32.26] are shown in Figure 32.8 (a) and (b). The first *Case-1* cluster shown in part (a) of Figure 32.8 is a C_4 type (0_4) cluster (A_1, T_1, E) which was solved in Table 32.6. The other *Case-1* cluster shown in part (b) is a C_3 type ($\pm 1_3$) cluster (T_1, E, T_2). (Recall C_3 correlations in Figure 32.3) They are similar to the corresponding sketches shown in Figure 32.7 (e). One notable difference is that inversion doublet shows little or no splitting in the (A_1, T_1, E) cluster but does split in the (T_1, E, T_2) cluster.

When the tunneling rates fall below ten or twenty kilohertz the angular momentum could remain near a particular C_3 or C_4 symmetry axis for a time that is longer than the nuclear spin precession rates. Spin precession rates and corresponding hyperfine splittings are on the order of fifty kilohertz and increasing with K. Hence there would be plenty of time for each of the nuclear spins to align or anti-align with the C_3 or C_4 symmetry axes of rotation. The resulting coupling is called *Case-2* coupling and the resulting spectra resembles that of an NMR scan of the nuclei with the magnetic field provided by the molecule itself through its own body frame rotation.

If SiF$_4$ rotates uniformly on one C_4 symmetry axis then all four F-nuclei occupy equivalent positions that are the same distance on the average from the rotation axis and experience the same local magnetic fields. The molecule is like a paired diatomic F$_2$-F$_2$ rotor with each one symmetrized or antisymmetrized so as to make the whole state symmetric. Table 32.6 shows the spin-$^1/_2$ base states listed horizontally by total projection I_z of nuclear spins on the C_4 axis. Horizontal arrays ($\uparrow\downarrow$) of spins denote symmetric states while vertical arrays ($\genfrac{}{}{0pt}{}{\uparrow}{\downarrow}$) denote antisymmetric spin states. This symmetry analysis is expanded in following Sections.

The hyperfine energy is approximately proportional to the projection I_z. The resulting spectrum is (1,2,4,2,1)-degenerate pyramid of equally spaced lines as shown in Figure 32.8 (c). Four spin-$^1/_2$ states without symmetry restrictions would give the standard binomial (1,4,6,4,1)-degeneracy seen in NMR spectra.

$I_z = 2$	$I_z = 1$	$I_z = 0$	$I_z = -1$	$I_z = -2$
		$\left\|\begin{matrix}\uparrow & \uparrow \\ \downarrow & \downarrow\end{matrix}\right\rangle$		
		$\|\uparrow\downarrow\ \uparrow\downarrow\rangle$		
	$\|\uparrow\downarrow\ \uparrow\uparrow\rangle$	$\|\downarrow\downarrow\ \uparrow\uparrow\rangle$	$\|\downarrow\downarrow\ \uparrow\downarrow\rangle$	
$\|\uparrow\uparrow\ \uparrow\uparrow\rangle$	$\|\uparrow\uparrow\ \uparrow\downarrow\rangle$	$\|\uparrow\uparrow\ \downarrow\downarrow\rangle$	$\|\uparrow\downarrow\ \downarrow\downarrow\rangle$	$\|\downarrow\downarrow\ \downarrow\downarrow\rangle$

Table 32.6 Hyperfine spin states

If the molecule settles upon C_3 symmetry axes of rotation the situation is markedly different. The four nuclei no longer occupy equivalent positions. One nucleus sits on the rotation axis while the other three nuclei occupy equivalent positions that are off the axis. The off-axis nuclei experience a different local magnetic field than the lone on-axis nucleus. (See Figure 32.8 (d).) From the spectrum it appears that the spin-up to spin-down energy difference is much greater for the lone on-axis nucleus than it is for the three equatorial nuclei. The spin states for the three equatorial nuclei form an energy quartet of spin states. . The lone on-axis nucleus has an energy doublet with a large splitting, so together the four nuclei give a doublet of quartets as shown in the figure.

If the off-axis nuclei had experienced the greatest splitting then the spectrum could have been a quartet of doublets instead of a doublet of quartets. Such effects also appear in superhyperfine structure of SF_6 analyzed below. For either of these molecules it is remarkable how different the rovibrational 'chemical shifts' can become for equivalent symmetry sites. The result is a microscopic example of spontaneous symmetry breaking.
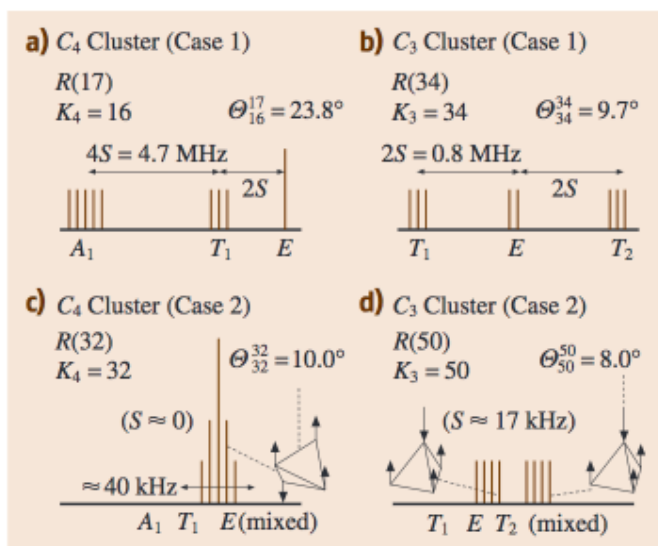

Fig. 32.8a−d Stick sketches for example of superfine and hyperfine spectral structure found by *Pfister* [32.26]; (a),(b) Case 1 clusters (high tunneling amplitude S); (c),(d) Case 2 clusters (low tunneling amplitude S)

32.5.3 Large spherical top molecules: Cubic-octahedral symmetry effects

The most common high symmetry molecules belong to either the tetrahedral T_d or cubic-octahedral O or O_h groups. The T_d group of order 24 matches order $^\circ S_4 = 4!$ of CF_4 nuclear permutation. O_h symmetry is more complicated. The octahedral O_h molecule SF_6 has F-spin-$\frac{1}{2}$ permutation symmetry S_6 of order $6! = 720$, 15 times larger than O_h. This allows O_h species to be correlated with a supercluster of S_6 symmetries that define nuclear spin hyperfine multiplets just as each C_4 or C_3 subgroup species correlate in Fig. 32.6 with a cluster of O_h symmetries.

Borde' *et.al.*[32.27,28,29] first resolved hyperfine structure in *10μm v_3* bands of SF_6. Fig. 32.9 displays *16μm v_4* bands [32.30] with focus on P(88) fine structures in part (b) that contain superfine clusters in part (c) that in turn have hyperfine (d) and super-hyperfine structure (e). Like CF_4 spectra in Fig. 32.7, SF_6 v_4P(N)-cluster bands avoid P(N±1) neighbors, while SF_6 v_3P(N)-bands are crowded together by having lower scalar Coriolis splitting factors ($\zeta_3 < \zeta_4$) or greater tensor cluster splitting factors ($\tau_3 > \tau_4$). [32.31,32,33]

Fig. 32.9 SF_6 *16μm v_4 P(88) spectral clusters for C_4 axis rotation on left and C_3 axis on right.*

In either case, a symmetry correlation is done in Fig. 32.10 between O_h subgroup species $\{A_{1g}, \ldots, T_{2u}\}$ and super-group S_6 species labeled by 6-box spin-$\frac{1}{2}$ Young tableaus of 1 or 2 rows. Pauli-Fermi antisymmetry matches each spin tableau to its conjugate spatial tableau of 1 or 2 columns. Each matched pair belongs to a total nuclear spin of $I=0$ (singlet state), $I=1$ (triplet), $I=2$ (quintet), or $I=3$ (septet). This is correlated with one or more of the 7 allowed O_h subgroup species $\{E_u, T_{1g}, T_{1u}, T_{2g}, A_{1g}, A_{1u}, A_{2u}\}$ and 3 species E_g, T_{2u}, and A_{2g} are forbidden. They would be allowed if F-spin were greater than $\frac{1}{2}$. If F-spin is less, i.e., *zero*, then only A_{1g} is allowed.

Case-1 hyperfine SF$_6$ spectra are sketched in center and lower right boxes of Fig. 32.9d-e as was done for CF$_4$ in Fig. 32.7d-e. Case-1 has greater superfine cluster splitting *between* O_h species than spin multiplet splitting *within* them as seen by comparing these boxes to Fig. 32.10.
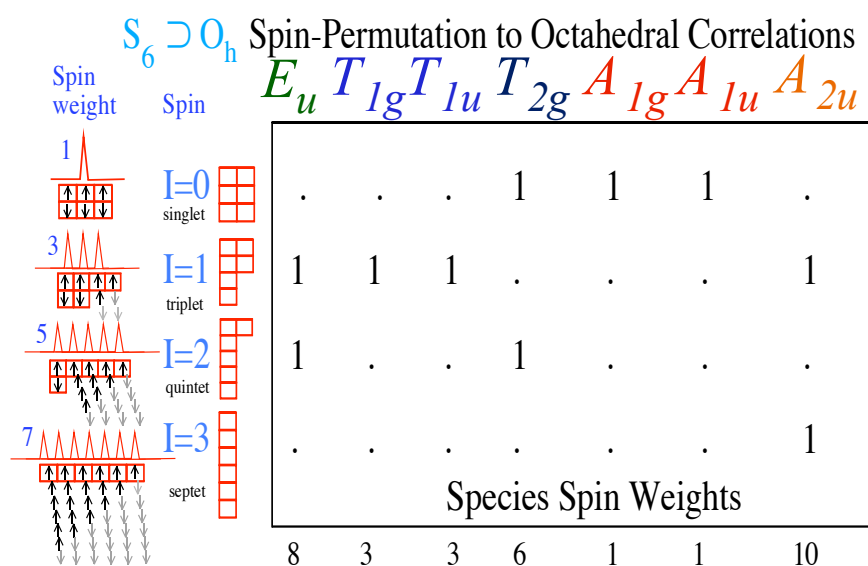
Fig. 32.10 SF$_6$ *states of nuclear spin I=0-3 correlated with* O_h *symmetry species listed on top.*

The lowest A_2 boxes hold an (I=1) triplet and (I=3) septet for spin-weight 10 below A_{2u} in Fig. 32.10. Above that lie T_{2g} boxes with an (I=0) singlet and (I=2) quintet (weight 6), E_u with an (I=1) triplet and (I=2) quintet (weight 8), T_{1g} or T_{1u} triplet boxes, and finally A_{1g} or A_{1u} singlets.

To form an SF$_6$ molecule requires considerable spontaneous symmetry breaking to make six F atoms, free to undergo (at the very least) 6! permutations, settle into O symmetry around a Sulfur atom that has only 24 permutations. (A full $O_h \subset S_6$ correlation valid for any Fermi or Bose XY$_6$ octahedral molecule is given in Ref. [32.31]) Thus, SF$_6$ spectra in Fig. 32.9 involves a more severe symmetry downfall than that of CF$_4$ in Fig. 32.7.

This kind of downfall amounts to a breakdown of Herzberg's rule concerning rovibronic spin species: *Transitions between species are very strictly forbidden since the nuclear moments are so very slight.* [32.2,3]In other words, if sub-kilo-Hertz interactions are negligible between states separated by MHZ or GHz then resonant mixing of different species is unlikely.

However, it was only found later how symmetric molecules have tight level clusters that force sub-kilo-Hertz near-degeneracy such as $6 \cdot 10^{-12}$Hz for A_1T_1E cluster $n_4=88$ in Fig. 32.9c. Here the exponential die-off of intra-cluster tunneling causes Case-2 superhyperfine mixing of species in a range from $n_4=88$ down to about $n_4=78$ where sub-kHz splitting begins. Also, on the righthand side of Fig. 32.9c, the C_3 clusters labeled by $n_3=88$ and 87 may fall into Case 2, too.

When O_h species levels such as the A_2T_2E cluster $n_4=86=2\ mod\ 4$ in Fig. 32.9c are crushed together, the corresponding energies and states mix and reorganize as shown in Fig. 32.11. With $O{\subset}S_6$ symmetry of Case-1, all six O-axes $\{x\bar{x}y\bar{y}z\bar{z}\}$ are equivalent. The three cluster levels are labeled by O_h symmetry species A_{2u} (lowest $\mathbf{J}$-tunneling energy: H-$4S$), T_{2g} (middle: H), and E_u (highest H+$2S$) and their 6-box S_6 tableaus correlated by Fig. 32.10 columns A_{2u}, T_{2g}, and E_u. The columns match each O_h species to one or two spin multiplets. A_{2u} is the winner with the highest hyperfine weight of 10: (I=3)-septet+(I=1)-triplet that gives a Borde A_{2u} spectra like the one shown on the lower righthand side of Fig. 32.11. (Note that the Borde spectral curve is a derivative of the seven peaks. Ideally seven *zeros* of that curve precisely locate septet *peaks*.)

The middle Case-1 T_{2g} has the lowest spin weight of 6: (I=2)-quintet+(I=0)-singlet with an easily read Borde spectrum of 5 peaks and central peak doubled. The top E_u has a spin weight of 8: (I=2)-quintet+(I=1)-triplet with a more confusing Borde spectrum, possibly due to onset of Case-2 mixing that happens if *ATE* splitting S is approaching that of hyperfine multiplets.

When the 6-axis $\mathbf{J}$ tunneling rate S goes to zero, the SF$_6$ becomes stuck to rotating on single axis pair $\{z\bar{z}\}$ so four F-atoms rotate around the equator while the other two take up a more sedate residence at North (z) and South (-z) poles. Such restriction of freedom or symmetry breaking is indicated symbolically by literally breaking the six-box tableaus of S_6 into four-box and two-box pairs labeling subgroups of $S_4{\otimes}S_2$ or $D_4{\otimes}C_2$. Each orbit tableau is Fermi-matched to a conjugate spin tableau (Recall Fig. 32.10) as shown on Case-2 level side of Fig. 32.11.

The whirling 4-box nuclei enjoy greater spin-rotation coupling than their sedate 2-box cohorts. To flip one of their 4 spins from ↓ to ↑ takes more energy than to flip a 2-box spin. (The Borde spectra in Fig. 32.11 indicate about 4 times more.) So raising ↓↓↓↓ to ↑↑↑↑ costs the entire width of the super hyperfine pattern while raising ↓↓ to ↑↑ costs only a triplet width. The scalar paired 2-box spins ↑↓ and 4-box spins ↑↑↓↓ are invariants.
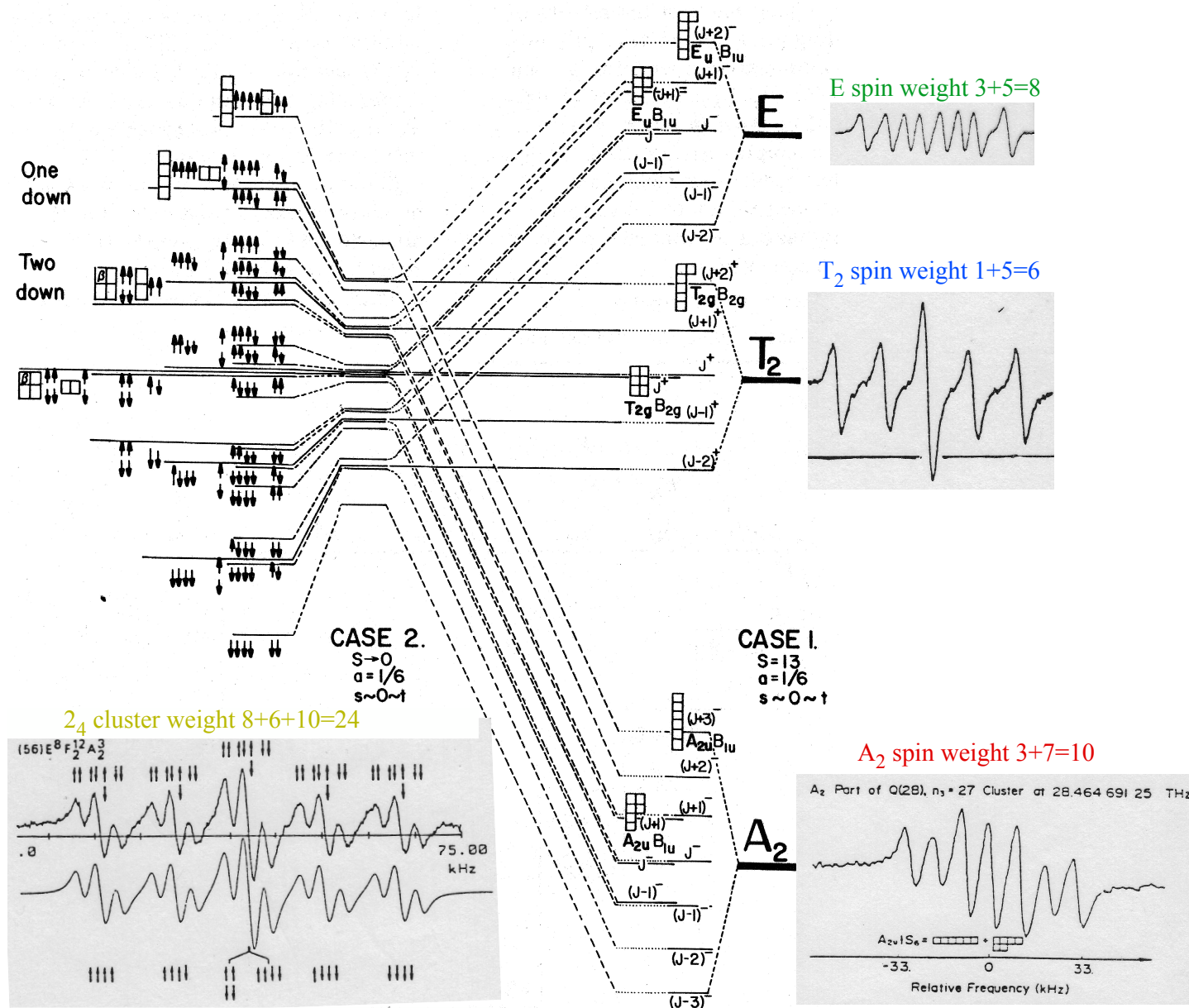
Fig. 32.11 *Case-1* $S_6 \supset O\{A_2 T_2 E\}$ *levels mix to become Case-2* $C_{4v} \otimes C_{2h}$ *superhyperfine levels.*

[*Spectra: J. Borde and Ch. Borde, Chem. Phys. 71, 471 (1982); Theory: Harter, Phys. Rev. A 24, 192(1981)*]

32.5.4 Icosahedral spherical top molecules: Extreme spin symmetry effects

Until the discovery of fullerenes and the structure of virus capsids, molecules with the highest icosahedral symmetry were thought to be rare or non-existent in nature. [32.34,35] With discovery of Buckminsterfullerene (Buckyball) C_{60} with molecular point symmetry Y_h or I_h one expects extreme dynamical symmetry effects. It helps to compare Y_h-symmetric C_{60} to the O_h-symmetric SF_6 first by their symmetry-allowed rotation Hamiltonians of lowest rank. [32.36,37]

$$\mathbf{H}_{SF_6}^{Rot} = B_{SF_6}\mathbf{J}^2 + t_{044}\left(\sqrt{\tfrac{7}{12}}\mathbf{T}_0^{(4)} + \sqrt{\tfrac{5}{24}}\left(\mathbf{T}_{+4}^{(4)} + \mathbf{T}_{-4}^{(4)}\right)\right) + \dots \qquad (32.18a)$$

$$\mathbf{H}_{C_{60}}^{Rot} = B_{C_{60}}\mathbf{J}^2 + t_{066}\left(\sqrt{\tfrac{11}{25}}\mathbf{T}_0^{(6)} + \sqrt{\tfrac{7}{25}}\left(\mathbf{T}_{+5}^{(6)} + \mathbf{T}_{-5}^{(6)}\right)\right) + \dots \qquad (32.18b)$$

Both have large rotor inertia I and small rotor constant $B = \tfrac{1}{2I}$. (For C_{60}:$2B = 0.0056$ cm^{-1} or 168 MHz. For SF_6:$2B$=.091 cm^{-1}) [32.38] Both use Wigner-Eckart form for tensor matrix elements.

$$\left\langle {}_{K'}^{J}\left|\mathbf{T}_q^{(k)}\right|{}_{K}^{J}\right\rangle = C_{qKK'}^{kJJ}(J \parallel k \parallel J) \qquad (32.18c)$$

$J=30$ eigenvalues of $\mathbf{H}_{SF_6}^{Rot}$ in Fig. 32.4 are to be compared to $J=100$ values of $\mathbf{H}_{C_{60}}^{Rot}$ in Fig. 32.12. Six C_4 hills of $\mathbf{H}_{SF_6}^{Rot}$ RES (Rotational Energy Surface) compare to 12 C_5 hills on $\mathbf{H}_{C_{60}}^{Rot}$ RES and 8 C_3 valleys of $\mathbf{H}_{SF_6}^{Rot}$ RES compare to 20 C_3 valleys on $\mathbf{H}_{C_{60}}^{Rot}$ RES. C_3 cut-off angle $\theta_3^{cut\text{-}off}$=10.8° for $\mathbf{H}_{C_{60}}^{Rot}$ is half of 19.5° for $\mathbf{H}_{SF_6}^{Rot}$. So the huge $J=100$ manifold has room for only two C_3 clusters.

A first comparison of SF_6 and $^{13}C_{60}$ assumes Fluorine and ^{13}C nuclei causes no hyperfine splitting. (Here we ignore Fig. 32.11 and assume C_{60} rotates slowly with ^{13}C magnetic moments too weak to observe.) Just as order is maintained in a sequence of SF_6 species between C_3 valleys and C_4 hills in Fig. 32.4, so also is the order of $^{13}C_{60}$ symmetry species maintained as C_3 valley clusters morph into C_5 hill clusters on either side of the separatrix in Fig. 32.12b.

While SF_6 or $^{13}C_{60}$ level sequence is maintained their intra-and-inter-cluster level *spacing* is not. C_3 *valley* intra-cluster level *spacing* in Fig. 32.12c is quite different from the C_5 *hill* intra-cluster level *spacing* in Fig. 32.12d, and similarly for SF_6 cluster level eigenvalues in Table 32.5. Intra-cluster (superfine) eigenvalues have a quasi-exponential tunneling "sneak" factor S that was first defined for the asymmetric rotor by eq.(32.13). It depends on local angular momentum m_n of each C_n cluster and J-momentum cone polar angle $\Theta_{m_n}^J$ as diagrammed by Fig. 32.5.

$$\Theta_{m_n}^J = \mathrm{acos}\frac{m_n}{\sqrt{J(J+1)}} \qquad (32.19)$$

Asymmetric-rotor eigenvalues in Table 32.1 and CF_4 or SF_6 eigenvalues in Table 32.5 have numerical rationality that contrasts with the irrationality of C_{60} Golden ratios (G^+=$(1+\sqrt{5})/2$ and $\sqrt{13}$ of superfine eigenvalues in Fig. 32.12(c-d). Rational frequencies give Poincare periodicity while irrational ones give quasi-periodicity.

However, discussion of similarity of SF_6 and $^{13}C_{60}$ ends when the hyperfine structure of the latter overwhelms that of the former. This is revealed in the following section.
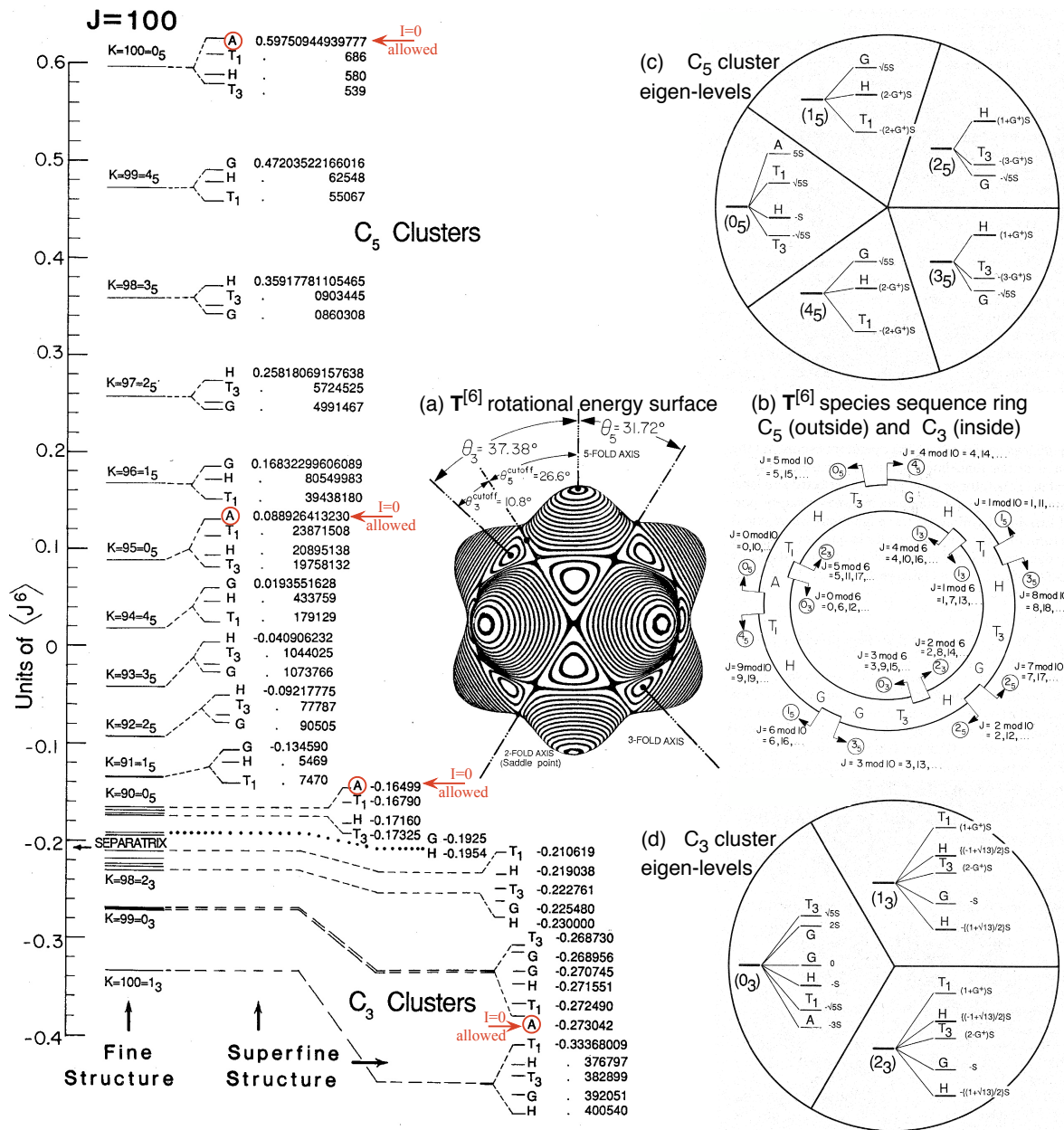
Fig. 32.12 J=100 Y_h-symmetry sub-levels. $^{12}C_{60}$ allows only the four A-species. $^{13}C_{60}$ allows all.
(a) $T^{[6]}$ RES of 26.6° C_5 hills or 10.8° C_3 valleys hold (b-c) many C_5 levels and (d) few C_3 levels.

3*2.5.5* *$^{12}C_{60}$ versus $^{13}C_{60}$: A world of difference in spin-½ hyperfine spectroscopy*

SF_6 has one stable F-isotope. C_{60} chooses from two stable C isotopes; ^{12}C (spin 0) of 98.9% abundance or ^{13}C (spin-$\frac{1}{2}$) at 1.1%. ^{12}C spectroscopy is simpler than that of ^{13}C. (The ^{14}C spin-0 isotope is even more tricky with its 5,707yr-half-life β-decay into ^{14}N.) It helps to compare purely Bosonic $^{12}C_{60}$ with purely Fermionic $^{13}C_{60}$. In between are many mixed $^{12}C_n{}^{13}C_{60-n}$ isotopomers. The first $^{12}C_{59}{}^{13}C$ is 33% likely and is an extreme example of isotopic symmetry breaking.[32.39] A *single extra neutron* reduces the very highest 3D point symmetry Y_h (120 operators) down to a lowly C_h (one planar reflection). [32.40]

After comparing levels of SF_6 and $^{13}C_{60}$ above one should also compare SF_6 (J=30) levels in Fig. 32.4 to *allowed* $^{12}C_{60}$ (*J=100*) levels in Fig. 32.12. Only *four* of its *201* levels are Bose-allowed A-species: $K=n_5=100$, $K=n_5=95$, $K=n_5=90$, and finally $K=n_3=99$, in the second to lowest cluster in the C_3 valley. The upper three are $K=0$-mod-5=0_5 waves orbiting C_5 hills. $K=n_3=99$ is the only 0-mod-3 wave in the tiny C_3 valley of the RES and thus the valley's only $^{12}C_{60}$-allowed level in Fig. 32.12.

Clearly, $^{12}C_{60}$ has a very sparse fine structure. This helps spectroscopists to assign lines and determine $^{12}C_{60}$ constants that will approximate those of $^{13}C_{60}$. (If $^{12}C_{60}$ has molecular weight of 720 atomic units then $^{13}C_{60}$ weighs in around 780.) Recently, (as this article was being written) the very first *J*-resolved $^{12}C_{60}$ spectra was observed in its *8.4μm v_2* bands by Jun Ye's group at JILA[32.41] that pioneered direct frequency comb spectroscopy. In this work they used cavity-enhanced comb spectroscopy along with buffer gas cooling. [32.42] This follows 27 years of failed attempts by other labs around the world. Now it suggests that a "Mt. Everest" of molecular spectroscopy, namely the $^{13}C_{60}$ spin-monster, might be attainable.

There is both good and bad news concerning this. The good news: Fermi-symmetric $^{13}C_{60}$ has only ten times as many rotating spin-$^1/_2$ nuclei as SF_6. The bad news: That factor-of-10 lies in exponents!

So $^{13}C_{60}$ has about *2^{60}* hyperfine states or about *$1.15 \cdot 10^{18}$* spin states distributed among its 10 species [31] as listed in Fig. 32.13. That is in contrast to Bose-symmetric $^{12}C_{60}$ that has only a handful of A-states in each J-multiplet. Yet a single neutron entering $^{12}C_{60}$ to form $^{12}C_{59}{}^{13}C$ causes many of the excluded levels to arise under lower C_h symmetry labels.

SF_6 spin-weights {8,3,3,6,1,1,10} in $O_h \subset S_6$ correlation of Fig. 32.10 fit a sum identity of O_h irep dimension $\ell^{(\mu)}$ times each of its spin-weights. This equals its total spin dimension 2^6=64.

$$8 \cdot \ell^{E_u} + 3 \cdot \ell^{T_{1u}} + 3 \cdot \ell^{T_{1g}} + 6 \cdot \ell^{T_{2g}} + 1 \cdot \ell^{A_{1g}} + 1 \cdot \ell^{A_{1u}} + 10 \cdot \ell^{A_{2u}}$$
$$= 16 \quad + 9 \quad + 9 \quad + 18 \quad + 1 \quad + 1 \quad + 10 = 64 = 2^6$$

<div align="right">(32.20)</div>

A similar identity uses products of U(2) spin-$\frac{1}{2}$ dimensions (2S+1) with ireps of group S_6 whose tableaus match U(2) tableaus that belong to each total spin S=3,2,1,0 made by six spin-$\frac{1}{2}$ nuclei.

$$2^6 = \ell_{U(2)}^{\square\square\square\square\square\square} \ell_{S_6}^{\square\square\square\square\square\square} + \ell_{U(2)}^{\square\square\square\square\square} \ell_{S_6}^{\square\square\square\square\square} + \ell_{U(2)}^{\square\square\square\square} \ell_{S_6}^{\square\square\square\square} + \ell_{U(2)}^{\square\square\square} \ell_{S_6}^{\square\square\square} \tag{32.21}$$

$$= (2S+l=7)\cdot\ 1 \qquad + (2S+l=5)\cdot\ 5 \qquad + (2S+l=3)\cdot 9 \qquad + (2S+l=1)\cdot 5$$

Tableau hooklength-formulas give irep dimension for S_n and for U(m). (See [32.[15]] p.65)

$$\ell_{S_{15}}^{\square} = \frac{15!}{\text{hooklength}} \cdot \frac{1}{\text{product:}} \tag{32.22a}$$

$$\ell_{U(5)}^{\square} = \frac{\text{integer product:}}{\text{hooklength product:}} \tag{32.22b}$$

The *hooklength h* of a tableau box is the number n_r of boxes to its right plus the number n_b below it plus 1 for itself, that is $h= n_r+n_b+1$. Numerator for S_n formula (32.22a) is *n!* (Here *n*=15) Denominator has exactly *n*-boxes with one hook length for each particle. The same denominator applies to U(*m*) irep dimension (32.22b) for an *n*-particle-*m*-state system (Here *m*=5), but the numerator fills the same tableau frame with a matrix whose corner diagonal is (*m,m,m,…*), and ±1st off-diagonals are ±(*m±1,m±1, m±1…*), ±2nd off-diagonals are ±(*m±2,m±2, m±2…*), etc.

The (32.22) fractions always yield a positive integer if the desired representation exists and zero otherwise. U(2) fractions (*m*=2) derive factors $\ell_{S_6}^{[\mu]} = \{1,5,9,5\}$ in (32.20).

$$\ell_{S_6}^{[\mu]} = \{1,5,9,5\} = \left\{ \ell_{O_h}^{A_{2u}},\ \ \ell_{O_h}^{E_u} + \ell_{O_h}^{T_{2g}},\ \ \ell_{O_h}^{A_{2u}} + \ell_{O_h}^{E_u} + \ell_{O_h}^{T_{1g}} + \ell_{O_h}^{T_{1u}},\ \ \ell_{O_h}^{A_{1g}} + \ell_{O_h}^{A_{1u}} + \ell_{O_h}^{T_{2g}} \right\} \tag{32.23}$$

This is consistent with (32.21), (32.22) and the $O_h \subset S_6$ correlation table in Fig. 32.10 if we recall that each Fermi spin tableau has to be the *transpose* of its rotor tableau factor in order to make the Fermi-Dirac-Pauli totally antisymmetric spin-rotor state. The hook length formulae structure (32.22) shows that a tableau has the same dimensions as its transpose for both S_n and U(*m*).

As powerful as tableau formulae are, they do not quite prepare us for the huge tableau dimensions and correlations associated with $^{13}C_{60}$ and its permutation symmetry S_{60} containing its icosahedral symmetry subgroup $Y_h \subset S_{60}$. The analogous spin-weights in Fig. 32.13 for a $Y_h \subset S_{60}$ correlation are truly enormous numbers when compared to the analogous $O_h \subset S_6$ numbers in Fig. 32.10. Most C_{60} spin states have no Y or Y_h-symmetry. Applying all 60 Y operators to a typical state generally gives 60 orthogonal spin states spanning a 60-by-60 *regular representation* and reducing to $1A \oplus 3T_1 \oplus 3T_3 \oplus 4G \oplus 5H$ that obeys its group order sum relation.

$$°Y = (\ell^A)^2 + (\ell^{T_1})^2 + (\ell^{T_3})^2 + (\ell^G)^2 + (\ell^H)^2 = 1^2 + 3^2 + 3^2 + 4^2 + 5^2 = 60 \tag{32.24}$$

So Y_h species weights in Fig. 32.13 are (to 1 part in 10^6) proportional to irep dimension. Thus the approximate weight ratios are (A:T_1:T_3:G:H)=(1:3:3:4:5) with relatively tiny ratio

variations between odd (*u*) and even (*g*) parity species. However, as Fig. 32.13 shows, the arithmetic variations are in the billions! This is in contrast to SF$_6$ where *u* and *g* ratios of O$_h$ species differ markedly and even leave the three species A$_{2g}$, E$_g$, and T$_{2u}$ with *zero* weight.

A_g	9,607,679,885,269,312	$=$w(A_g)
	0 1 2 3 4 5 6 7 8 9 10 11 12 13 14 15	
A_u	9,607,678,793,631,424	$\sim$w(A_g)
T_{1g}	28,823,036,970,926,496	~ 3w(A_g)
	0 1 2 3 4 5 6 7 8 9 10 11 12 13 14 15 16	
T_{1u}	28,823,037,990,981,216	~ 3w(A_g)
T_{3g}	28,823,036,970,926,496	~ 3w(A_g)
T_{3u}	28,823,037,990,981,216	~ 3w(A_g)
G_g	38,430,716,856,193,728	~ 4w(A_g)
G_u	38,430,716,784,610,624	~ 4w(A_g)
H_g	48,038,396,740,938,240	~ 5w(A_g)
H_u	48,038,395,577,718,272	~ 5w(A_g)

Fig. 32.13 *Total spin weights and m_z-distributions for* Y$_h \subset$ S$_{60}$ *symmetry species*

Plots of species weight *vs* spin *z*-component ($-30 \le m_z \le 30$) are shown along the right hand side of Fig. 32.13. Height of each vertical line is proportional to the number of a given species A, T$_1$, T$_3$, G, or H that have the m_z value that line represents. Each species has its tallest line at $m_z = 0$ then falls quasi-exponentially on either side. They become too small to plot for m_z values outside the interval ($-12 \le m_z \le +12$) and thereafter are just lines of dots. The dots for scalar icosahedral A species at extreme values of $m_z = +30$ or $m_z = -30$ are lines of height $\ell^{[60,0]}=1$ for S$_{60}$ tableaus below. Dots for other species are zero at maximal spin momentum $|m_z|=30$.

$m_z=+30$

$$1\qquad 5\qquad 10\qquad 15\qquad 20\qquad 25\qquad 30\qquad 35\qquad 40\qquad 45\qquad 50\qquad 55\qquad 60 \qquad (32.25)$$

$m_z=-30$

The opposite extreme is the spin tableau [30,30] for totally paired-up zero-spin ($S=0=m_z$).

$$m_z=0 \qquad\qquad\qquad\qquad\qquad (32.26)$$

The S$_{60}$ dimension $\ell^{[30,30]}$ for this zero-spin tableau is given by applying (32.22a).

$$\ell^{[30,30]} = \frac{60 \cdot 59 \cdot 58 \cdot 57 \cdots 2 \cdot 1}{\begin{array}{c}31 \cdot 30 \cdot 29 \cdot 28 \cdots\cdots 3 \cdot 2 \\ 30 \cdot 29 \cdot 28 \cdot 27 \cdots\cdots 2 \cdot 1\end{array}} = \frac{60!}{(31!)(30!)} = 3.8149865020923 \cdot 10^{15} \qquad (32.27)$$

That number of zero-m_z states is apportioned by ratios 1:3:3:4:5 ($\pm 0.0001\%$) to species A, T_1, T_3, G, and H, respectively (Exact ratio calculation is tricky and required an erratum.[32.40]) If ever the resulting panoply of $^{13}C_{60}$ super-hyperfine spectra is observed it will dwarf that of SF_6 in Fig. 32.9 and Fig. 32.10. A plot comparing J=100 superfine levels of $^{13}C_{60}$ to those of $^{12}C_{60}$ in Fig. 32.12 only begins to relate to SF_6 levels in Fig. 32.4. An attempt to relate spectra of $^{13}C_{60}$ to $^{12}C_{60}$ is sketched by Fig. 32.14 as a highly speculative P(50) prognostication where only two A-singlet $^{12}C_{60}$ lines exist while $^{13}C_{60}$ has seven large clusters. The $(K=50)0_5(AT_1H\ T_3)$ cluster is a Case-1 guess for superfine structure of astronomical numbers of hyperfine lines. Resolution-assignment of such super-hyper-spectra will require a wealth of future technology and theory.
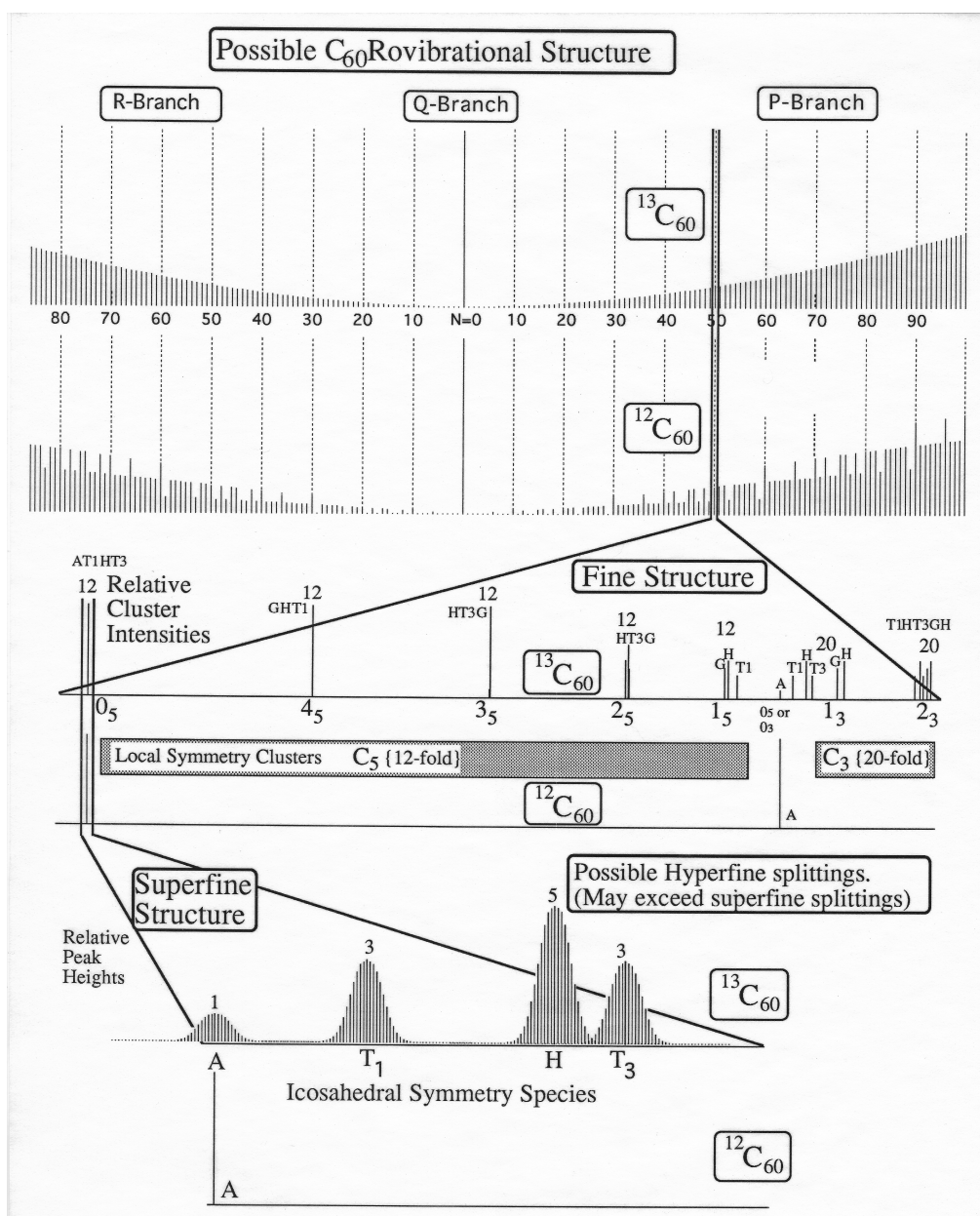
Fig. 32.14 Comparison sketch of possible P(50) spectral structure for $^{12}C_{60}$ and $^{13}C_{60}$.

32.6 Composite rotors and multiple RES

So far, the discussion has focused on Hamiltonians and RE surfaces involving functions of even mulipolarity, that is, constant *(k=0)*, quadratic or quadrupole *(k=2)*, quartic or hexadecapole *(k=4)*, while ignoring functions that are linear-dipole *(k=1)*, or cubic-octupole *(k=3)* for reasons of time-reversal symmetry. However, for composite "rotor-rotors" any mulitpolarity is possible and the dipole is of primary utility.

A composite rotor is one composed of two or more objects with more or less independent angular momenta. This could be a molecule with attached methyl (CH_3) "gyro" or "pinwheel" sub-rotors, a system of considerable biological interest. It could be a molecule with a vibration or "phonon" excitation that couples strongly to rotation. Also, any nuclear or electronic spin with significant coupling may be regarded as an elementary sub-rotor. The classical analogy is a spacecraft with gyro(s) on board.

A rotor-rotor Hamiltonian has the following general interaction form.

$$H_{rotor\ R+S} = H_{rotor_R} + H_{rotor_S} + V_{RS} \qquad (32.28)$$

A useful approximation assumes the rotor$_S$ "gyro" is fastened to the frame of rotor$_R$ so the interaction V_{RS} becomes a constraint, does no work, and is thus assumed zero. An asymmetric top with body-fixed spin is the following modified version of (32.1).

$$H_{R+S(Body-fixed)} = A\mathbf{R}_x^2 + B\mathbf{R}_y^2 + C\mathbf{R}_z^2 + H_{rotor_S} + (\sim 0) \qquad (32.29a)$$

The system total angular momentum is a conserved vector **J=R+S** in the lab-frame and a conserved magnitude |**J**| in the rotor-R body frame. So we use **R=J-S** in place of **R**.

$$
\begin{aligned}
H_{R,S(fixed)} &= A\left(\mathbf{J}_x - \mathbf{S}_x\right)^2 + B\left(\mathbf{J}_y - \mathbf{S}_y\right)^2 + C\left(\mathbf{J}_z - \mathbf{S}_z\right)^2 + H_{rotor_S} \\
&= A\mathbf{J}_x^2 + B\mathbf{J}_y^2 + C\mathbf{J}_z^2 - 2A\mathbf{J}_x\mathbf{S}_x - 2B\mathbf{J}_y\mathbf{S}_y - 2C\mathbf{J}_z\mathbf{S}_z + H'_{rotor_S}
\end{aligned}
\qquad (32.29b)
$$

Gyro-spin components $\mathbf{S_a}$ are treated at first as constant classical parameters S_a.

$$
\begin{aligned}
H_{R,S(fixed)} &= \text{const.}\mathbf{1} - 2AS_x\mathbf{J}_x - 2BS_y\mathbf{J}_y - 2CS_z\mathbf{J}_z + A\mathbf{J}_x^2 + B\mathbf{J}_y^2 + C\mathbf{J}_z^2 \\
&= M_0\mathbf{T}_0^0 \quad + \quad \Sigma_d D_d\mathbf{T}_d^1 \quad + \quad \Sigma_q Q_q\mathbf{T}_q^2
\end{aligned}
\qquad (32.29c)
$$

This is a simple Hamiltonian *multipole tensor operator expansion* having here just a monopole $\mathbf{T}_0^0$ term, three dipole $\mathbf{T}_a^1$ terms, and two quadrupole $\mathbf{T}_q^2$ terms shown in Fig. 32.15. Each is a radial plot of a spherical harmonic function $Y_q^k(\varphi, \vartheta)$ representing a tensor operator $\mathbf{T}_q^k$.
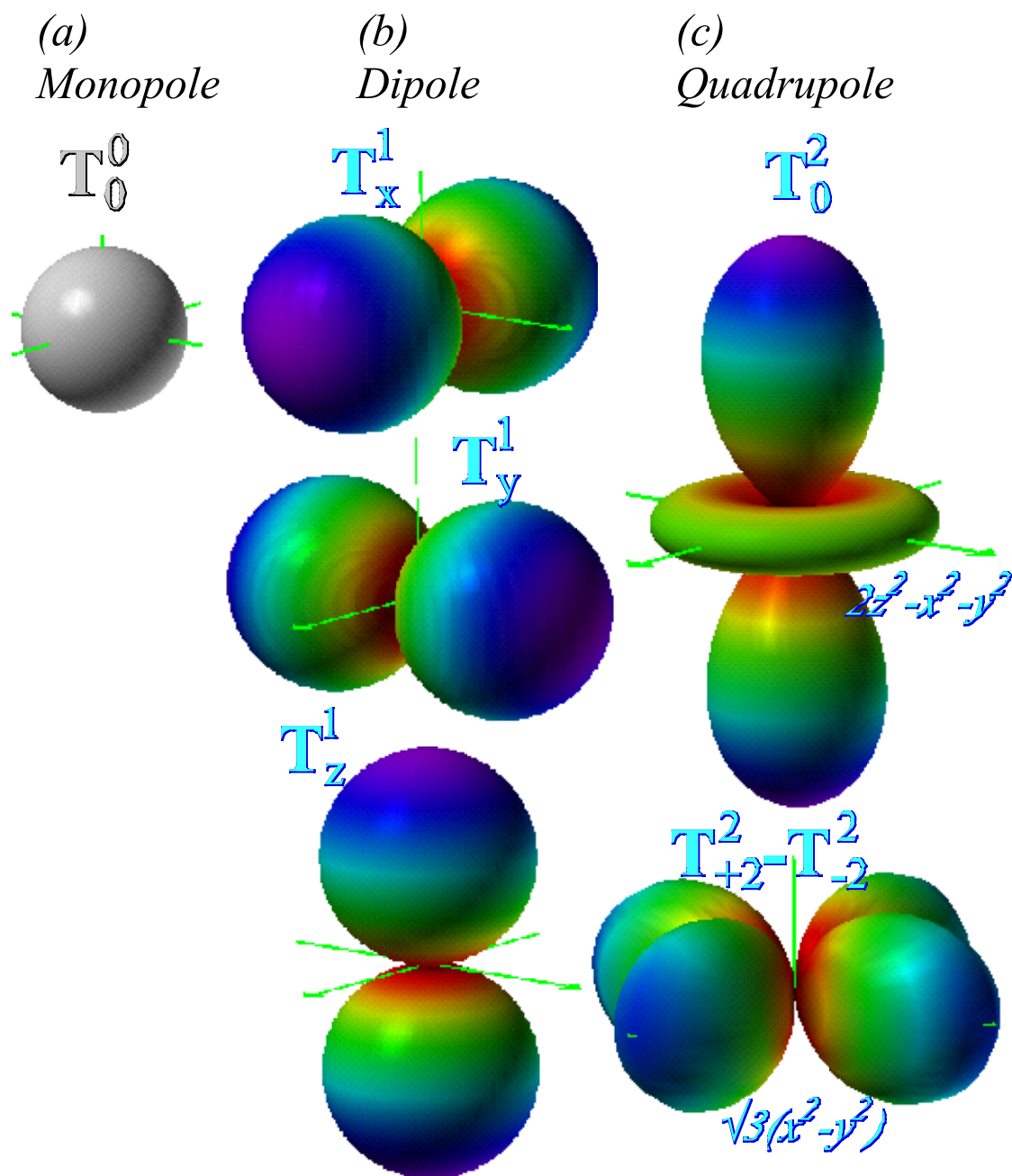
Fig. 32.15 The six lowest order RES components needed to describe rigid gyro-rotors.

$$\mathbf{T}_0^0 = \frac{\mathbf{J}_x^2 + \mathbf{J}_y^2 + \mathbf{J}_z^2}{3}$$

$$\mathbf{T}_x^1 = \mathbf{J}_x = \frac{\mathbf{T}_{+1}^1 + \mathbf{T}_{-1}^1}{\sqrt{2}}$$

$$\mathbf{T}_y^1 = \mathbf{J}_y = \frac{\mathbf{T}_{+1}^1 - \mathbf{T}_{-1}^1}{i\sqrt{2}}$$

$$\mathbf{T}_z^1 = \mathbf{J}_z = \mathbf{T}_0^1$$

$$\mathbf{T}_{zz}^2 = \frac{2\mathbf{J}_z^2 - \mathbf{J}_x^2 - \mathbf{J}_y^2}{2} = \mathbf{T}_0^2$$

$$\mathbf{T}_{x^2-y^2}^2 = \mathbf{J}_x^2 - \mathbf{J}_y^2 = \frac{2\left(\mathbf{T}_2^2 - \mathbf{T}_{-2}^2\right)}{\sqrt{6}}$$

(32.30a)   (32.30b)   (32.30c)

The constant coefficients or *moments* indicate strength of each multipole symmetry.

$$M_0 = A + B + C + 3H'_{rotor_S}$$

$$D_x = -2AS_x,$$
$$D_y = -2BS_y,$$
$$D_z = -2CS_z$$

$$Q_{zz} = \left(2C - A - B\right)/6$$
$$Q_{x^2-y^2} = \left(A - B\right)/2$$

(32.31a) \qquad\qquad (32.31b) \qquad\qquad (32.31c)

The scalar monopole RES (a) is a sphere, while vector dipole RES (b) are bi-spheres pointing along Cartesian axes, and the RES (c) resemble quadrupole antenna patterns. Also, Fig. 32.15(a-c) plot the six s, p, and d Bohr-Schrodinger orbitals that are analogs for the six octahedral J-tunneling states listed in Table 32.5.

The asymmetric and symmetric rotor Hamiltonians (32.1) and (32.2) are combinations of a monopole (32.30a) that, by itself makes a spherical rotor, and varying amounts of the two quadrupole terms (32.30c) to give the rigid rotor RES pictured previously in Fig. 32.1 and Fig. 32.2. Both Q-coefficients (32.31c) are zero for a spherical top *(A=B=C)* but only one is zero for a symmetric top *(A=B)*.

Combining monopole (32.30a) with dipole terms (32.30b) gives a gyro-rotor Hamiltonian (32.19b) for a spherical rotor *(A=B=C)* that has the following form.

$$H=const+ BJ^2 -g\mu\mathbf{S}\cdot\mathbf{J} \quad \text{(where: } -g\mu=2A=2B=2C\text{)} \qquad (32.32)$$

H resembles a dipole potential -**m·B** for a magnetic moment **m**=g**J** that precesses clockwise around a lab-fixed magnetic field **B**=μ**S**. (The PE is least for **J** along **S**.)

Here, the Hamiltonian (32.32) is a simple example of *Coriolis* rotational energy. It is least for **J** along **S** where |**R**|=|**J-S**| is least and rotor kinetic energy BR^2 is least. (Magnitudes |J| and |S| are constant here.) The spherical rotor-gyro RES in Fig. 32.16 is minimum along body axis +**S** and maximum along –**S** where BR^2 is greatest.

As is the case for rigid solid rotors in Fig. 32.1 and Fig. 32.2, the RES energy topography lines determine the precession **J**-paths in the body frame wherein gyro-**S** is fixed in Fig. 32.16. The left hand rule gives **J**-precession sense in the body **S**-frame, that is, all **J** precess *anti-clockwise* relative to the "low" on the +**S**-axis or clockwise relative to the "high" on the –**S**-axis. In the lab, **S** precess clockwise around a fixed **J**.

Gyro-RES differ from solid rotor RES that have two opposite "highs" and/or two opposite "lows" separated by saddle fixed points where the precessional flow direction reverses as seen in Fig. 32.2. The gyro-RES in Fig. 32.16 has no saddle fixed points and only one "high" and one direction of flow with the same harmonic precession frequency for all **J**-vectors between the high +**S** and low –**S**-axes.This is because the spectrum of the gyro-rotor Hamiltonian (25.A. 22) is *harmonic* or *linear* in the momentum quanta *K*.

$$\left\langle {J \atop K} \left| H \right| {J \atop K} \right\rangle = const. + BJ(J+1) - 2BK \qquad (32.33)$$

In contrast, even the symmetric rigid rotor spectrum (32.4) is *quadratic* in *K*. Other rotors shown in Fig. 32.2 and Fig. 32.4 have levels that are quite non-linear.
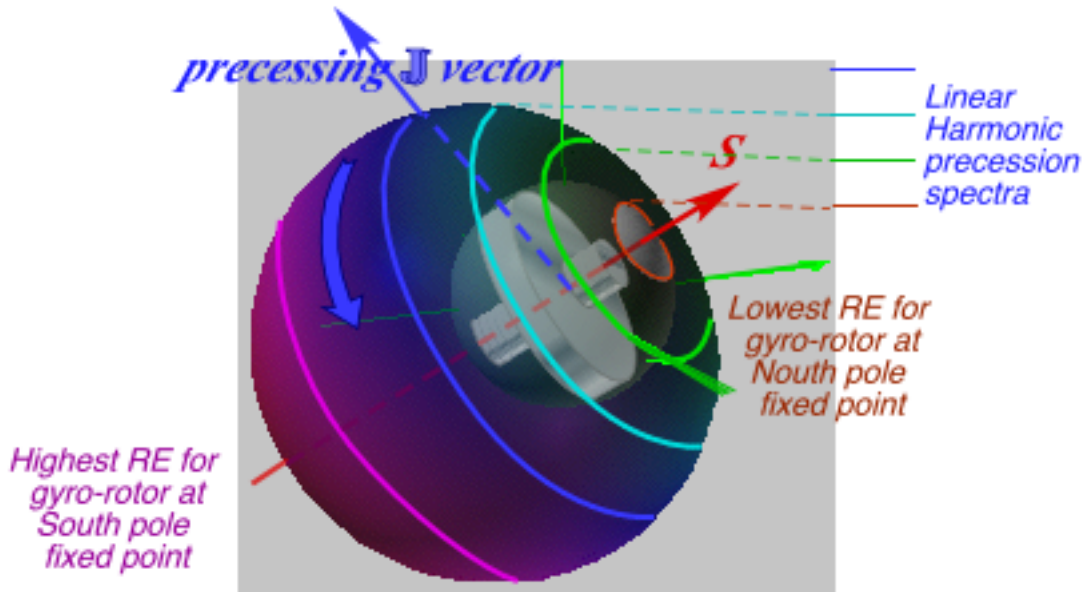
Fig. 32.16 The spherical gyro-rotor RES is a cardioid of revolution around gyro spin S

32.6.1 3D-Rotor and 2D-Oscillator Analogy

Linear levels belong to harmonic *oscillators* not rotors, but a gyro-rotor's linear spectrum highlights a 150-year-old analogy of 3D rotor motion to 2D vibration. Stokes [32.43] described 2D electric vibration or *optical polarization*, by a 3D vector later known as Stokes vector and labeled appropriately by the letter **S**. (Now we say **S** labels "spin.") Stokes' spin uses Hamilton *quaternions* [32.44,45], redone 80 years later as Pauli *spinor* σ_μ components [32.46] of a general 2D Hermitian operator H.

$$(32.34)$$
$$H = \begin{pmatrix} A & B - iC \\ B + iC & D \end{pmatrix} = \frac{A + D}{2}\sigma_0 + \frac{A - D}{2}\sigma_A + B\sigma_B + C\sigma_C,$$

$$\text{where: } \sigma_0 = \begin{pmatrix} 1 & 0 \\ 0 & 1 \end{pmatrix}, \ \sigma_A = \begin{pmatrix} 1 & 0 \\ 0 & -1 \end{pmatrix}, \ \sigma_B = \begin{pmatrix} 0 & 1 \\ 1 & 0 \end{pmatrix}, \ \sigma_C = \begin{pmatrix} 0 & -i \\ i & 0 \end{pmatrix}.$$

Our labels: *A ("Asymmetric-diagonal"), B ("Bilateral-balanced"), and C("Circular-Coriolis")* are mnemonic alternatives to Pauli's z, x, and y, respectively. The 2D Hamiltonian has the **S·J** form of the Coriolis coupling (32.32).

$$H = S_0\mathbf{1} + S_A J_A + S_B J_B + S_C J_C = S_0 J_0 + \vec{S} \bullet \mathbf{J}, \ (32.35)$$

$$\text{where: } J_0 = \mathbf{1}, \quad J_A = \frac{\sigma_A}{2}, \quad J_B = \frac{\sigma_B}{2}, \ J_C = \frac{\sigma_C}{2},$$

$$\text{and: } S_0 = (A + D)/2, \ S_A = (A - D), \ S_B = 2B, \quad S_C = 2C.$$

The 2D-3D analogy is helped by using elementary oscillator ladder $a^\dagger a$ operators.

$$\mathbf{J_0} = \mathbf{N} = a_1^\dagger a_1 + a_2^\dagger a_2, \ \mathbf{J}_A = \frac{1}{2}\left(a_1^\dagger a_1 - a_2^\dagger a_2\right), \ \mathbf{J}_B = \frac{1}{2}\left(a_1^\dagger a_2 + a_2^\dagger a_1\right), \ \mathbf{J}_C = \frac{-i}{2}\left(a_1^\dagger a_2 - a_2^\dagger a_1\right).$$

$$(32.36)$$
$$\text{where: } a_1^\dagger a_1 = \begin{pmatrix} 1 & 0 \\ 0 & 0 \end{pmatrix}, \ a_1^\dagger a_2 = \begin{pmatrix} 0 & 1 \\ 0 & 0 \end{pmatrix}, \ a_2^\dagger a_1 = \begin{pmatrix} 0 & 0 \\ 1 & 0 \end{pmatrix}, \ a_2^\dagger a_2 = \begin{pmatrix} 0 & 0 \\ 0 & 1 \end{pmatrix}.$$

This is a Jordan-Schwinger map of 2D oscillation to 3D rotation. [32.47,48,49]

This easily gives Schwinger's 3D angular momentum raising-lowering operators

$\mathbf{J}_+ = \mathbf{J}_B + i\mathbf{J}_C = a_1^\dagger a_2$ and $\mathbf{J}_- = \mathbf{J}_B - i\mathbf{J}_C = a_2^\dagger a_1$, where 2D dimensions *1* and *2* are *spin-up (+ℏ/2)* and *spin-down (-ℏ/2)* instead of *x*-and *y*-polarized states envisioned by Stokes.

Angular 3D ladder operation is replaced by a simpler 2D oscillator operations.

$$\mathbf{J}_+ \left| n_1 n_2 \right\rangle = a_1^\dagger a_2 \left| n_1 n_2 \right\rangle = \sqrt{n_1 + 1}\sqrt{n_2}\left| n_1 + 1, n_2 - 1 \right\rangle$$
$$\mathbf{J}_- \left| n_1 n_2 \right\rangle = a_2^\dagger a_1 \left| n_1 n_2 \right\rangle = \sqrt{n_1}\sqrt{n_2 + 1}\left| n_1 - 1, n_2 + 1 \right\rangle \quad (32.37)$$

2D oscillator states are labeled by *total* number $N=(n_1+n_2)$ of quanta and the *net* quantum population $\Delta N=(n_1-n_2)$. 3D angular momentum states $\left| {J \atop K} \right\rangle$ are similarly labeled by total momentum $J=N/2=(n_1+n_2)/2$ and z-component $K=\Delta N/2=(n_1-n_2)/2$, just half (or ℏ/2) of N and ΔN.

$$\left| n_1, n_2 \right\rangle = \frac{\left(a_1^\dagger\right)^{n_1}\left(a_2^\dagger\right)^{n_2}}{\sqrt{n_1! n_2!}}\left| 0,0 \right\rangle = \left| {J \atop K} \right\rangle = \frac{\left(a_1^\dagger\right)^{J+K}\left(a_2^\dagger\right)^{J-K}}{\sqrt{(J+K)!(J-K)!}}\left| 0,0 \right\rangle, \text{ where:} \begin{cases} n_1 = J + K \\ n_2 = J - K \end{cases} \quad (32.38)$$

From this Schwinger [32.48] re-derived the Wigner matrices $D_{MK}^J\left(\alpha\beta\gamma\right)$ appearing in (32.5) and (32.6) and Clebsch-Gordan $C_{qKK'}^{kJ\,J'}$ coefficient or Wigner-Eckart tensor relations. This helps clarify RES approximations such as (32.10) and (32.11) that use (J,K)-cone levels on RES.

$$\left\langle {J' \atop K'} \right| T_q^k \left| {J \atop K} \right\rangle = C_{qKK'}^{kJ\,J'}\left\langle J' \| k \| J \right\rangle \sim C_{0KK}^{kJ\,J}\left\langle J \| k \| J \right\rangle \sim D_{JK}^J\left(\Theta_K^J\right).$$

32.6.2 Gyro-Rotors and 2D-Local Mode Analogy

The 2D-3D analogy provides insight into NMR spin [32.50], laser quasi-spin (Rabi-rotation) [32.51], rovibrational dynamics [32.52,53], and local mode formation [32.54,5555]. It also has computational value. Part of this involves relating single 2D oscillator (Stokes model) to a model of two 1D oscillators with coordinates $x_1=x$ and $x_2=y$.

Two identical side-by-side oscillators have bilateral or *B*-symmetry and a H_B Hamiltonian commutes with both σ_B (a +45° mirror reflection of axes $\pm x \rightleftarrows \pm y$) and with -σ_B (a -45° mirror reflection of axes $\mp x \rightleftarrows \pm y$) both of which interchange oscillators.

This means that to first order the Hamiltonian *is* $H_B=2B\sigma_B$, that is, a gyro rotor T_x^1 with $\mathbf{S}$ along the *B*-axis as shown in Fig. 32.17. (Added $\mathbf{T}_0^0$ affects eigen*values*, not states.)

Eigenvectors of H_B are the symmetric and antisymmetric *normal modes* that belong to the fixed points on the $\mathbf{S}$-vector and $\pm B$-axes of the Stokes space. If instead, the $\mathbf{S}$-vector lies on the *A*-axis, the Hamiltonian is an asymmetric diagonal $H_A= 2A\sigma_A$ matrix. From (32.34) we see that operator σ_A reflects *y* into –*y* but leaves *x* alone, so eigenvectors of H_A are localized on the *x*-oscillator or the *y*-oscillator but not both. Such motions are *local modes*, but are not modes of H_B, which does not commute with H_A.

Hamiltonian H_B precesses a $\mathbf{J}$-vector from +*A*-axis (local *x*-mode) around to the –*C* axis to the –*A* (local *y*-mode), then to the+*C* axis, and then home to +*A*. The $\mathbf{J}$-path is the largest

equator of Fig. 32.17(a). The $\pm C$-axes are what Stokes would label *circular* polarization with chirality right and left, respectively. In a *B*-beat, $\pm C$ belong to resonant transitions where one vibrator's phase is $90°$ ahead and pumping up the other.

Simple mode beat transfer dynamics is disrupted by adding anharmonic $\mathbf{T}_0^2$ or $\mathbf{T}_{\pm 2}^2$ terms to existing *B*-symmetry terms $\mathbf{T}_x^1$ and $\mathbf{T}_0^0$, as shown in Fig. 32.17(b-c).
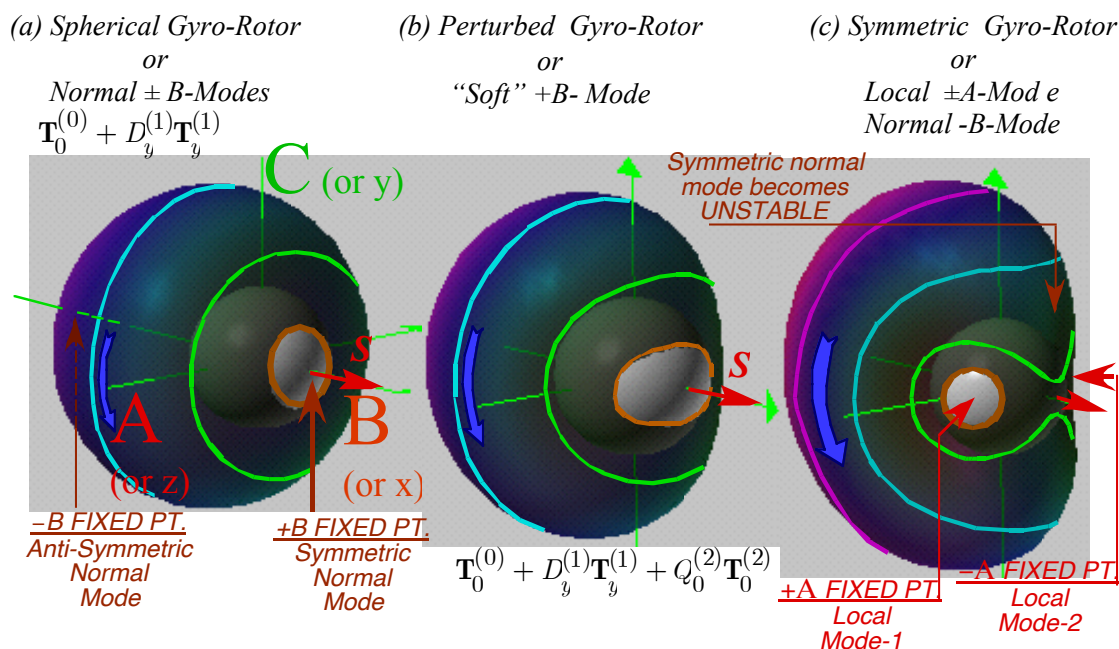

(a) Spherical Gyro-Rotor
or
Normal $\pm$ B-Modes
$\mathbf{T}_0^{(0)} + D_y^{(1)}\mathbf{T}_y^{(1)}$

(b) Perturbed Gyro-Rotor
or
"Soft" +B- Mode

(c) Symmetric Gyro-Rotor
or
Local $\pm$A-Mod e
Normal -B-Mode

$\mathbf{T}_0^{(0)} + D_y^{(1)}\mathbf{T}_y^{(1)} + Q_0^{(2)}\mathbf{T}_0^{(2)}$

Fig. 32.17 A spherical gyro-rotor becomes a symmetric gyro-rotor by adding $\mathbf{T}_0^2$.

In molecular rotation theory, the $\mathbf{T}_0^2$ term along with $\mathbf{T}_0^0$ make the initial unperturbed Hamiltonian (32.3) of a symmetric top, and gyro terms $\mathbf{T}_q^1$ are viewed as perturbations. For vibration theory, the latter make up a normal mode Hamiltonian and the former $\mathbf{T}_0^2$ term is viewed as an anharmonic perturbation.

The effect of $\mathbf{T}_0^2$, seen in Fig. 32.17(c), is to replace the stable fixed point $+B$ (representing the (+)-normal mode) by a saddle point as *B* bifurcates (splits) into a pair of fixed points that head toward the $\pm A$-axes. So one normal mode dies and begats two stable local modes wherein one mass may keep its energy without losing it to the other through the usual *B*-beating process. (The *A*-modes become anharmonically *detuned*.)

Pairs of classical modes that each localize energy on one side of an RES in Fig. 32.17 are analogous to asymmetric top $\pm K$-precession pairs in Fig. 32.2. However, one must consider more than the classical aspects of RES pictures. Quantum-tunneling Hamiltonians such as (32.15) give a superfine doublet for each trajectory pair with ($\pm$)-combination eigenstates (Recall Table 32.1), and they occupy *both* paths just as each gyro-spin doublet would have **J** both up *and* down the *A*-axis in a quantum picture.

32.6.3 Multiple Gyro-Rotor RES and Rotational Energy Eigen-surfaces (REES)

Just as quantum rotor theory allows **J** to occupy multiple paths so also may **J** occupy multiple RES. In this way gyro-rotors differ from the analogous **J** precession around a lab-fixed **B**-field or around the body-fixed **S** of a classical gyro. By allowing the **S** to be a quantum entity, the possibility arises for distribution over multiple RES. [32.56,57]

A simple quantum theory of **S** allows both **+S** and **-S** at once. The RES for each is plotted one on top of other as in Fig. 32.18 (a) while component RES are shown in Fig. 32.18(b) for **+S** and in Fig. 32.18(c) for **-S**. An energy sphere is shown intersecting an RES pair for an asymmetric gyro-rotor. If the spin **S** is set to zero, the pair of RES collapse to a rigid asymmetric top RES shown in Fig. 32.2. having angular inversion (time-reversal **J**→-**J**) and reflection symmetry. The composite RES in Fig. 32.18(a) has inversion symmetry but lacks reflection symmetry. Its parts in Fig. 32.18 (b) and in Fig. 32.18 (c) have neither symmetry due to their body-fixed gyro-spins ±**S**.

(a) Composite ±S Rotational Energy Surface

(b) Forward gyro-spin +S=(1,1,1)

(c) Time reversed gyro -S=(-1,-1,-1)
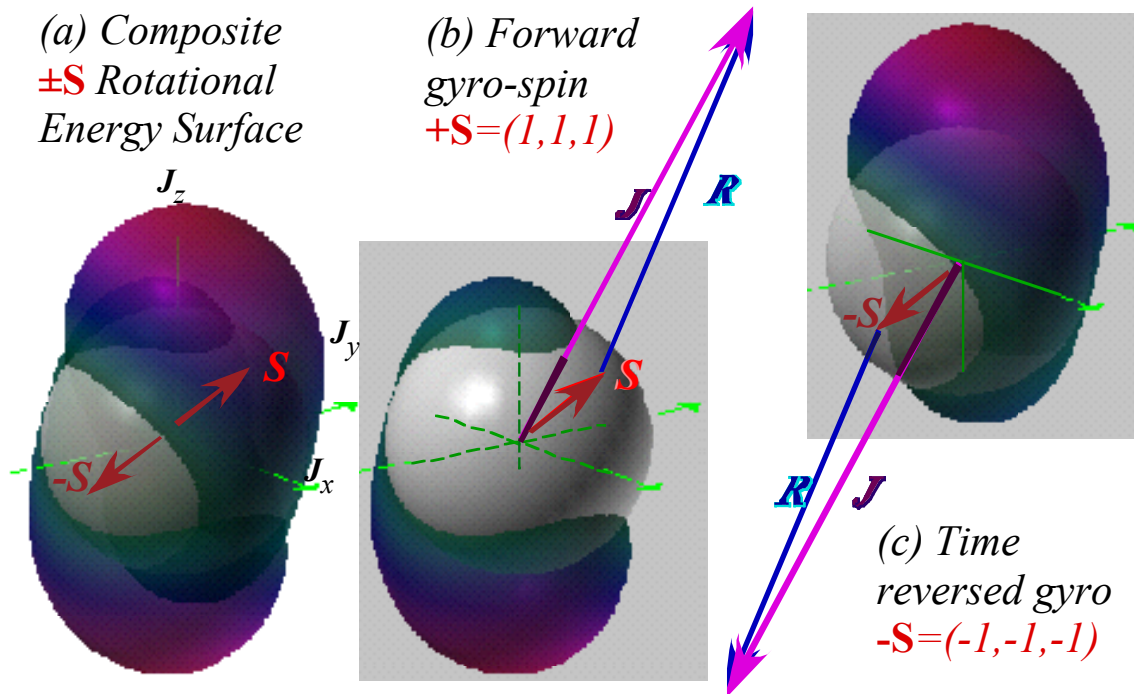
Fig. 32.18 Asymmetric gyro-rotor RES. . (Classical body-fixed-spin case.)
(a) Composite ±**S**. (b) Forward spin ± **S**. (c) Reversed spin – **S**.

Gyro-rotor Hamiltonians (32.39) allow tunneling or mixing of multiple RES. A two-state spin-*1/2* gyro-spin model has a *2-by-2* Hamiltonian matrix and two base-RES.

$$H_{gyro} = M_0 \mathbf{J \cdot J} + D_x S_x \mathbf{J}_x + D_y S_y \mathbf{J}_y + D_z S_z \mathbf{J}_z + Q_{xx} \mathbf{J}_x^2 + Q_{yy} \mathbf{J}_y^2 + Q_{zz} \mathbf{J}_z^2 \qquad (32.39)$$

As in eq. (32.7), **J** is approximated by classical vector components in the body frame.

$$\left(J_x = |J| \sin \beta \cos \gamma, \quad J_y = |J| \sin \beta \sin \gamma, \quad J_z = |J| \cos \beta \right) \qquad (32.40a)$$

But, the gyro spin S uses its quantum representation $\mathbf{S} = |S| \sigma/2 = \sqrt{3} \sigma/2$ from eq. (32.34).

$$\left\langle H_{gyro} \right\rangle = M_0 J^2 + Q_{xx} J_x^2 + Q_{yy} J_y^2 + Q_{zz} J_z^2 + D_x |S| \sigma_x J_x + D_y |S| \sigma_y J_y + D_z |S| \sigma_z J_z$$

$$= \begin{pmatrix} h(J) + D_z |S| J_z & |S| \left(D_x J_x - i D_y J_y \right) \\ |S| \left(D_x J_x + i D_y J_y \right) & h(J) - D_z |S| J_z \end{pmatrix} = \begin{pmatrix} h(J) + d_z \cos \beta & \left(d_x \cos \gamma - i d_y \sin \gamma \right) \sin \beta \\ \left(d_x \cos \gamma + i d_y \sin \gamma \right) \sin \beta & h(J) - d_z \cos \beta \end{pmatrix} \quad (32.40b)$$

where: $\qquad h(J) = M_0 J^2 + Q_{xx} J_x^2 + Q_{yy} J_y^2 + Q_{zz} J_z^2 \quad$ and: $\quad d_\mu = D_\mu |S||J| \qquad (32.40c)$

The semi-classical H_{gyro} makes spin expectation $\left\langle \mathbf{S} \right\rangle$ to precess around an angular velocity crank-vector Ω with the following **J**-dependent body frame components.

$$\left(\Omega_x = d_x \sin \beta \cos \gamma, \quad \Omega_y = d_y \sin \beta \sin \gamma, \quad \Omega_z = d_z \cos \beta \right) \qquad (32.40c)$$

A quantum REES shown in Fig. 32.20 results from substituting quantum spin $\mathbf{S} = \frac{1}{2}\sigma$ matrices $\frac{1}{2}\sigma_x$, $\frac{1}{2}\sigma_y$, or $\frac{1}{2}\sigma_z$ in for each algebraic Hamiltonian factor S_x, S_y, and S_z of (32.39) to make a matrix Hamiltonian (32.40) that is then diagonalized. The resulting pair of eigenvalues are plotted to make a pair of REES functions of polar body frame angles β and γ.

In comparing the classical composite RES in Fig. 32.18a or Fig. 32.19 with the quantum REES in Fig. 32.20 one may note that have similar shapes in regions where classical $\pm$J-surfaces of Fig. 32.19 are well separated. Wherever the classical RES cross the quantum REES differ most markedly due to their inter-surface resonance.

Each REES resembles a warped asymmetric top RES that is most perturbed at points where the two classical RES cross. The RES pair intersection along the horizontal x-axis (in figure plane) becomes an REES avoided crossing. The RES pair intersection along the y-axis (out of figure plane) becomes an REES *diabolical* point so-named after a toy top called a diablo. A current term for such a dual-cone singularity is *Dirac point*.

Near-crossing RES are the rotational equivalent of near-crossing vibrational-potential (VES) employed in treatments of Jahn-Teller effects [32.58,5959] The classical, semi-classical and quantum theory for such loosely bound or fluxional systems is a rapidly growing sub field of atomic, molecular, and optical physics.
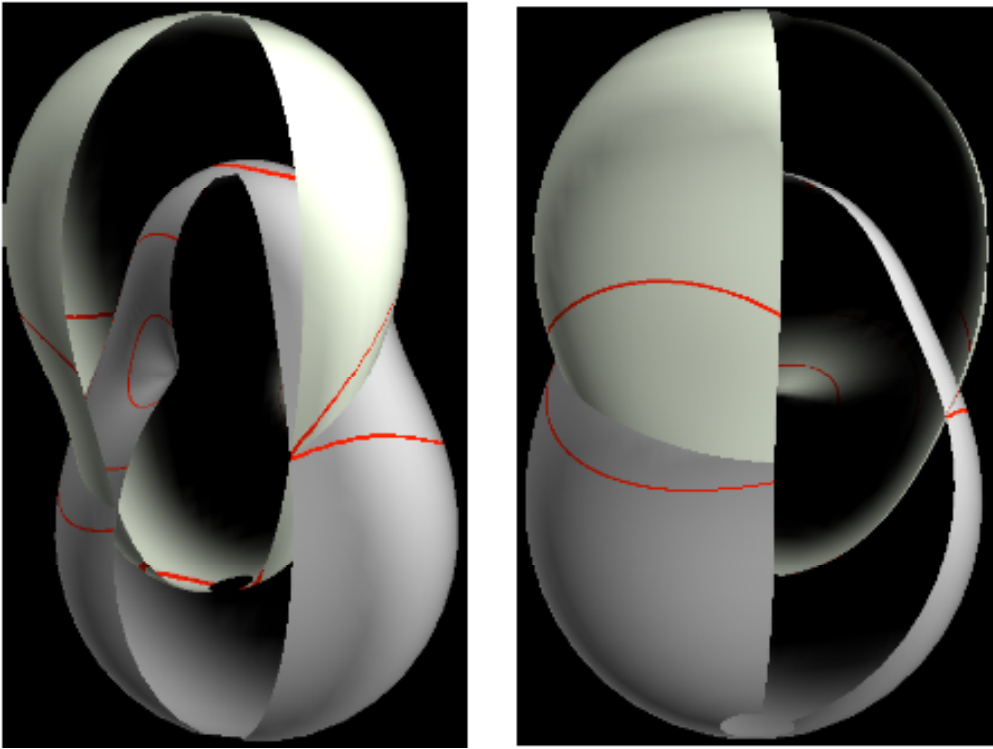
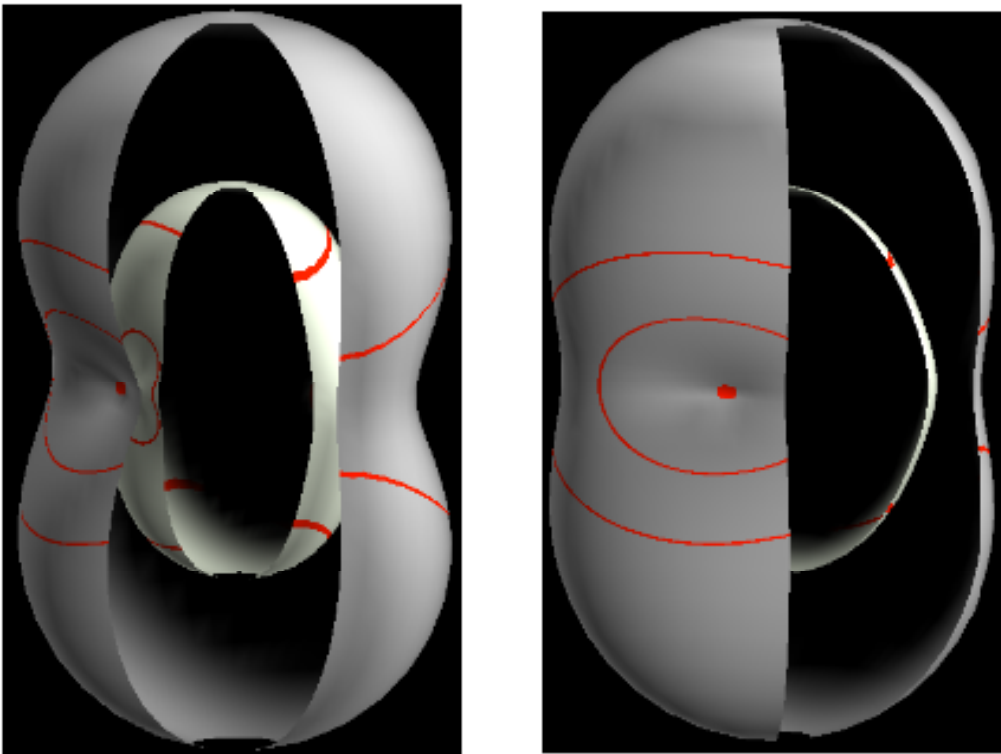*Fig. 32.19 Classical gyro-rotor c-RES views of Fig. 32.18 (a) based on (32.39).*

*Fig. 32.20 Quantum gyro-rotor REES views based on eigenvalues of (32.40) with **S**=σ/2.*

32.6.4 Multi-quantum CF$_4$ rovibrational polyads and REES visualization

Molecular quantum data comes first in the form of spectral line frequencies that are correlated with theory derived from Hamiltonian energy operator eigenvalues or differences thereof. Second comes a much larger data set that includes spectral transition rates and intensities that are correlated with eigenvector matrices or density operators. As more AMOP phenomena become available researchers try to understand this deluge of data and find ways to visualize it. Section 32.4 provides a theory for level-clustering of octahedral and tetrahedral molecules and shows a way to visualize underlying eigenstates using rotational energy surfaces (RES).

A possibility for visualizing ever more complex spectral phenomena involves rovibronic energy eigenvalue surfaces (REES) introduced in preceding section 32.6.3. An example involves the CF$_4$ $\nu_3/2\nu_4$ rovibrational polyad. It begins with a plot versus total angular momentum J=0-70 in Fig. 32.21 of level cluster bands found in this polyad as calculated by Boudon et. al. [32.60,61]

The plot uses squares($\square$) as boundary points containing C$_4$-level clusters such as are shown in Fig. 32.4(right) and C$_4$-correlated in Fig. 32.6(right). Triangular points($\triangle$) mark bands of C$_3$-clusters shown in Fig. 32.4(left) and C$_3$-correlated in Fig. 32.6(left).

Fig. 32.21 also has C$_2$-cluster regions marked by diamond ($\lozenge$) points where C$_2$-correlated species in Fig. 32.6(center) might appear. These are rare in O$_h$ or T$_d$ spectra as their RES have saddle points at their C$_2$ axes as in Fig. 32.4 so they are unstable. The asymmetric rotor in Fig. 32.2 is a prime example of an RES with unstable C$_2$ $\pm y$-saddle points.

However, overtone and combination resonances give rise to the larger clusters that have lower local symmetry of C$_2$ and C$_1$ (no symmetry). The $\nu_3/2\nu_4$ REES for (J=57)-states has 5 of its 9 shells showing in Fig. 32.22.[32.62] The innermost and lowest REES shell is nearly spherical at the scale of figure and corresponds to the lowest cluster levels in Fig. 32.21 that, if expanded, would reveal usual ordering C$_3$-below-C$_4$ separated by C$_2$ saddle as in Fig. 32.4. The shell above that has a cubic (as opposed to octahedral) shape with inverted ordering C$_4$-below-C$_3$ clearly shown by levels in the next-to-lowest J=57 cluster bunch in Fig. 32.21.

The three highest REES shells shown in Fig. 32.22 involve a level-cluster mash-up at the middle of Fig. 32.21. A pair of shells form diabolic points on C$_2$ axes and avoided-crossing pairs of orbits on both C$_3$ and C$_4$ axes. Above that is an extraordinary REES shell with 24 C$_1$ orbits indicated by arrows emerging from their loops. This 5th shell also supports many C$_3$ orbits, a few C$_4$ orbits, and a bizarre saddle shape on the C$_2$ axes.

The 24-cluster of C$_1$ orbits belongs to species correlation $0_1\uparrow O=A_1\oplus A_2\oplus E\oplus T_1\oplus T_2$ of a *regular* representation of the isomorphic groups S$_4$~T$_d$~O that now uses the identity subgroup C$_1$={**1**}. The relevant C$_1$, C$_2$, C$_3$, and C$_4$, correlation tables are matched to corresponding cluster orbits in Fig. 32.22. While each of the 24 C$_1$ orbits lack rotational symmetry they each do maintain a local reflection symmetry C$_v$={**1**, $\boldsymbol{\sigma_v}$}. At much higher J one should expect to find O$_h$ clusters of 48 species levels, indeed, a *majority* of them in analogy to the majority of regular S$_{60}$ spin states of unit S$_1$ symmetry in the correlation table of Fig. 32.13.
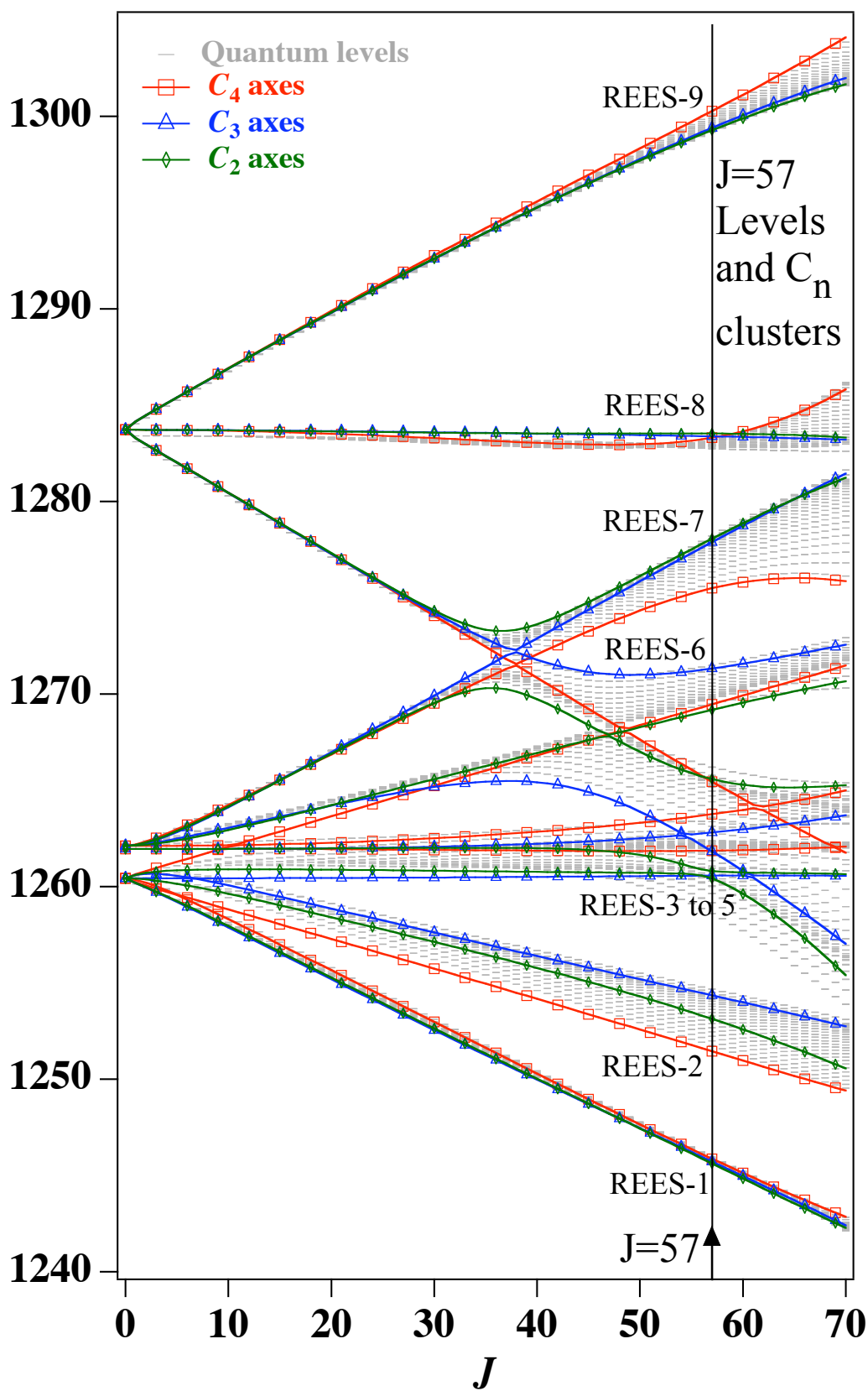
Fig32.21 CF$_4$ Molecular rovibrational level-clusters for $\nu_3/2\nu_4$ polyad J=0 to J=70
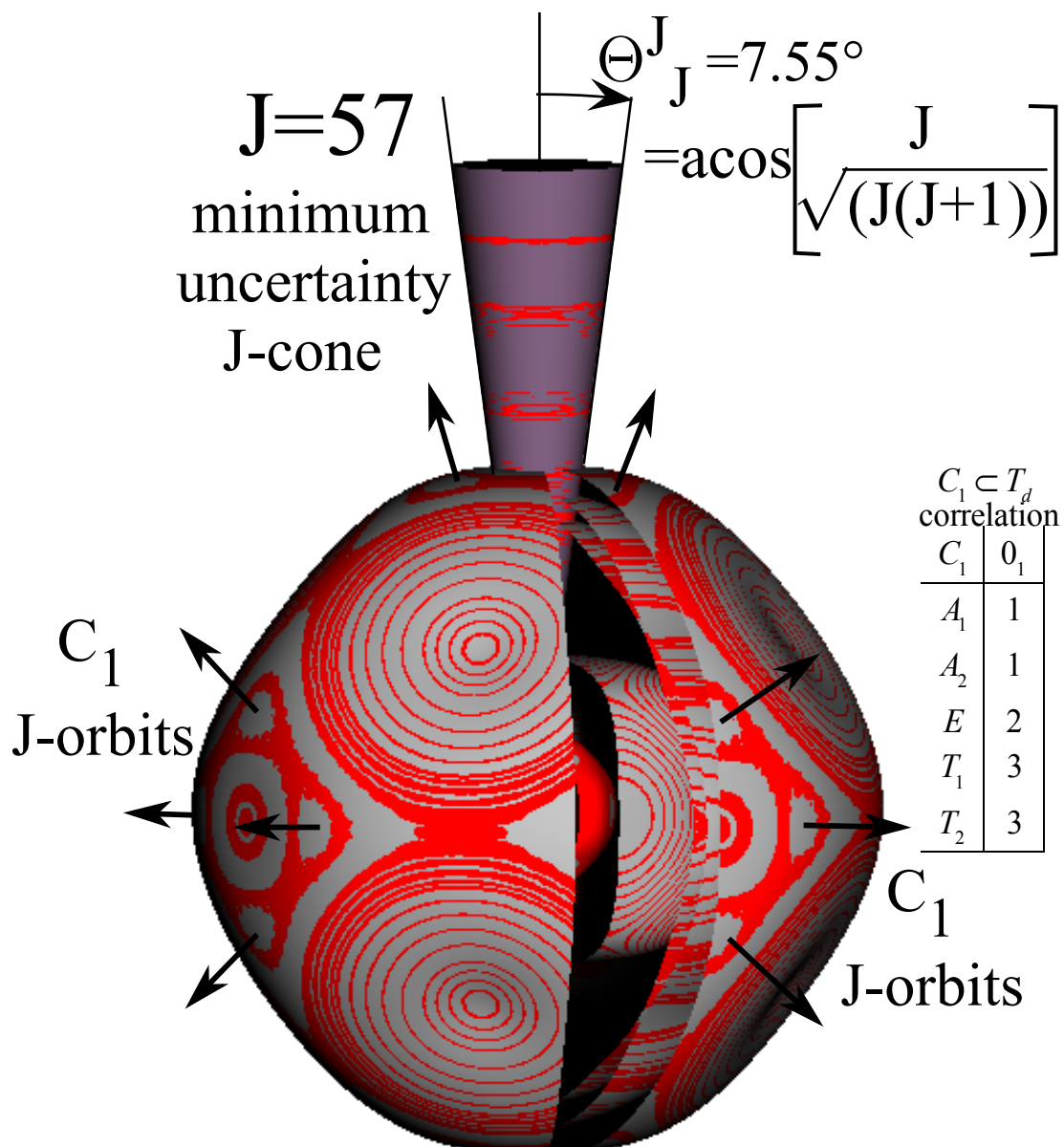Adapted from Boudon [32.60] . Energy units are 1 Kayser (1 cm^{-1}).

$$\Theta^J_J = 7.55° = \text{acos}\left[\sqrt{\frac{J}{(J(J+1))}}\right]$$

J=57
minimum
uncertainty
J-cone

C_1
J-orbits

C_1
J-orbits

$C_1 \subseteq T_d$ correlation	
C_1	0_1
A_1	1
A_2	1
E	2
T_1	3
T_2	3

Fig. 32.22 CF$_4$ Molecular (J=57) REES-1-to-5 for $\nu_3/2\nu_4$ polyad levels plotted in Fig. 32.21. Adapted from Harter and Mitchell, Int. J. Mol. Sci.[32.62]

References

32.1   G. Herzberg: *Molecular Spectra and Structure: Vol. I, Spectra of Diatomic Molecules* (Van-Norstrand–Reinhold, New York 1950)

32.2   G. Herzberg: *Molecular Spectra and Structure: Vol. II, Infrared and Raman Spectra of Polyatomic Molecules* (Van-Norstrand-Reinhold, New York 1945)

32.3   G. Herzberg: *Molecular Spectra and Structure: Vol. III, Electronic Structure of Polyatomic Molecules* (Van-Norstrand-Reinhold, New York 1966)

32.4   F. B. Wilson, V. C. Decius, P. C. Cross: *Molecular Vibrations* (McGraw Hill, New York 1955)

32.5   D. Papousek, M. R. Aliev: *Molecular Vibrational-Rotational Spectra, Studies Phys. Theor. Chem. 17* (Elsevier, Amsterdam 1982)

32.6   R. N. Zare: *Angular Momentum: Understanding Spatial Aspects in Chemistry and Physics* (Wiley Interscience, New York 1988)

32.7   W. G. Harter: *Principles of Symmetry, Dynamics, and Spectroscopy* (Wiley Interscience, New York 1993)

32.8   W. G. Harter, C. W. Patterson: J. Math. Phys. **20**, 1453 (1979)

32.9   W. G. Harter: Phys. Rev. A **24**, 192 (1981)

32.10 W. G. Harter, C. W. Patterson: J. Chem. Phys. **80**, 4241 (1984)

32.11 W. G. Harter: Comp. Phys. Rep. **8**, 319 (1988)

32.12 D. A. Sadovskii, B. I. Zhilinskii: Mol. Phys **65**, 109 (1988)

32.13 D. A. Sadovskii, B. I. Zhilinskii: Phys. Rev. A **47**, 2653 (1993)

32.14 I. M. Pavlichenkov: Phys. Rep. **226**, 173 (1993)

32.15 W. G. Harter, C. W. Patterson, F. J. daPaixao: Rev. Mod. Phys. **50**, 37 (1978)

32.16 W. G. Harter, C. W. Patterson: Phys. Rev. A **19**, 2277 (1979)

32.17 P. R. Bunker: *Molecular Symmetry and Spectroscopy* (Academic, New York 1979)

32.18 K. T. Hecht: J. Mol. Spectrosc. **5**, 355 (1960)

32.19 K. R. Lea, M. J. M. Leask, W. P. Wolf: J. Phys. Chem. Solids **23**, 1381 (1962)

32.20 A. J. Dorney, J. K. G. Watson: J. Mol. Spectrosc. **42**, 1 (1972)

32.21 K. Fox, H. W. Galbraith, B. J. Krohn, J. D. Louck: Phys. Rev. A **15**, 1363 (1977)

32.22 W. G. Harter, C. W. Patterson: J. Chem. Phys. **66**, 4872 (1977)

32.23 R. J. Butcher, Ch. Chardonnet, Ch. Bordé: Phys. Rev. Lett., **70**, 2698 (1993)

32.24 H. W. Kroto, J. R. Heath, S. C. O'Brian, R. F. Curl, R. E. Smalley: Nature **318**, 162 (1985)

32.25 W. Kratschmer, W. D. Lamb, K. Fostiropolous, D. R. Huffman: Nature **347**, 354 (1990)

32.26 O. Pfister: *Etude esperimentale et theorique des interactions hyperfines dans la bande de vibration ν_3 de la molecule $^{28}SiF_4$* (Dissertation, Univ., Paris-Nord 1993)

32.27 J. Bordé, Ch. J. Bordé: Chem. Phys. **71**, 417 (1982)

32.28 Ch. Bordé, J. Bordé, Ch. Breant, Ch. Chardonnet, A. Vanlerberghe, Ch. Salomon: *Laser Spectroscopy VII* (Springer, Berlin, Heidelberg 1985) p. 95

32.29 W. G. Harter, D. E. Weeks: Chem. Phys. Lett. **132**, 187 (1986)

32.30 D. E. Weeks, W. G. Harter: Chem. Phys. Lett. **144**, 366 (1988)

32.31 D. E. Weeks, W. G. Harter: Chem. Phys. Lett. **176**, 209 (1991)

32.32 W. G. Harter, T. C. Reimer: Chem. Phys. Lett. **194**, 230 (1992)

32.33 W. R. Hamilton: Proc. R. Irish Acad. II, 424 (1844)

32.34 W. R. Hamilton: Phi. Mag. **25**, 489 (1844)

32.35 G. Stokes: Proc. R. Soc. London **11**, 547 (1862)

32.36 W. Pauli: Z. Phys. **37**, 601 (1927)

32.37 P. Jordan: Z. Phys. **94**, 531 (1935)

32.38 J. Schwinger: *Quantum Theory of Angular Momentum*, ed. by L. C. Biedenharn, H. van Dam (Academic, New York 1965) p. 229

32.39 L. C. Biedenharn, J. D. Louck: *Angular Momentum in Quantum Physics*, Encyclopedia of Mathematics, Vol 8, ed. by G. C. Rota (Addison Wesley, Reading, Massachusetts 1981) p. 212

32.40 I. I. Rabi, N. F. Ramsey, J. Schwinger: Rev. Mod. Phys. **26**, 167 (1954)

32.41 R. P. Feynman, F. I. Vernon, R. W. Helwarth: J. Appl. Phys. **28**, 49 (1957)

32.42 W. G. Harter, N. dos Santos: Am. J. Phys. **46**, 251 (1978)

32.43 K. K. Lehmann: J. Chem. Phys. **79**, 1098 (1983)

32.44 W. G. Harter: J. Chem. Phys. **85**, 5560 (1986)

32.45 Z. Li, L. Xiao, M. E. Kellman: J. Chem. Phys. **92**, 2251 (1990)

32.46 W. G. Harter: Comp. Phys. Rep. **8**, 319 (1988), see pp. 378−85

32.47 J. Ortigoso, I. Kleiner, J. T. Hougen: J. Chem. Phys. **110**, 11688 (1999)

32.48 H. A. Jahn, E. Teller: Proc. R. Soc. London **A161**, 220 (1937)

32.49 H. A. Jahn, E. Teller: Proc. R. Soc. London **A164**, 117 (1938)

Older (2005) References are copied above to compare with current (2018) references below

(In Pages documents and some pdf's the current refs. are click connected to text.

Text references such as [32.34] clicks to ref. (34). Colored text ref. such as [32.34] is a repeat of
 a prior reference and will not respond to click action.)

[1] G. Herzberg:
Molecular Spectra and Structure: Vol. I, Spectra of Diatomic Molecules
(Van-Norstrand-Reinhold, New York 1950)

[2] G. Herzberg:
Molecular Spectra and Structure:Vol. II, Infrared and Raman Spectra of Polyatomic Molecules
(Van-Norstrand-Reinhold, NewYork 1945)

[3] G. Herzberg:
Molecular Spectra and Structure: Vol. III, Electronic Structure of Polyatomic Molecules
(Van-Norstrand-Reinhold, New York1966)

[4] F. B. Wilson, V. C. Decius, P. C. Cross:Molecular Vibrations
(McGraw Hill, New York 1955)

[5] D. Papousek, M. R. Aliev:Molecular Vibrational-Rotational Spectra, Studies
Phys. Theor. Chem17(Elsevier, Amsterdam 1982)

[6] R. N. Zare:Angular Momentum: Understanding Spatial Aspects in Chemistry and Physics
(Wiley Interscience, New York 1988)

[7] W. G. Harter:
Principles of Symmetry, Dynamics,and Spectroscopy
(Wiley Interscience, New York 1993)

[8] W. G. Harter, C. W. Patterson: J. Math. Phys. 20,1453(1979)

[9] W. G. Harter: Phys. Rev. A24,192(1981)

[10] W. G. Harter, C. W. Patterson: J. Chem. Phys.80, 4241 (1984)

[11] W. G. Harter: Comp. Phys. Rep.8,319(1988)

[12] D. A. Sadovskii, B. I. Zhilinskii: Mol. Phys 65,109(1988)

[13] D. A. Sadovskii, B. I. Zhilinskii: Phys. Rev. A47,2653(1993)

[14] I. M. Pavlichenkov: Phys. Rep. 226,173(1993)

[15] W. G. Harter, C. W. Patterson, F. J. daPaixao: Rev. Mod. Phys.50,37(1978)

[16] W. G. Harter, C. W. Patterson: Phys. Rev. A19,2277(1979)

[17] P. R. Bunker:Molecular Symmetry and Spectroscopy (Academic, New York 1979)

[18] K. T. Hecht: J. Mol. Spectrosc.5, 355 (1960)

[19] K. R. Lea, M. J. M. Leask, W. P. Wolf: J. Phys. Chem.Solids 23,1381(1962)

[20] A. J. Dorney, J. K. G. Watson: J. Mol. Spectrosc.42,1(1972)

[21] K. Fox, H. W. Galbraith, B. J. Krohn, J. D. Louck: Phys. Rev. A15,1363(1977)

[22] W. G. Harter, C. W. Patterson: J. Chem. Phys.66,4872 (1977)
W. G. Harter, C. W. Patterson: Phys. RevA19, 2277 (1979)

[23] B. Monostari, A. Weber, J. Chem Phys. 33, 1867(1960)

[24] A. Stein, P. Rabinowitz, and A. Kalder, Exxon Labs (1977)

[25] R.S. McDowell, H. W. Galbraith, M.J. Reisfeld, and J. P. Aldridge Los Alamos T-12
R. S. McDowell in Laser Spectroscopy III, ed. J. Hall and J. Carlsten, Springer (1977) p.102.

[26] O. Pfister:Etude esperimentale et theorique des interactions hyperfines dans la bande de
vibration v_3 de la molecule SiF_4 (Dissertation, Univ. Paris-Nord 1993)

[27] J. Borde, Ch. Borde, C.Salomon, A. VanLerberghe, M. Ouhayoun, and C.Cantrell
Laser Spectroscopy IV, ed. H. Walther and K. Rothe (Springer, Berlin 1975)

[28] J. Borde, Ch. Borde, J. Mol. Spectrosc. 78, 353 (1979)

[29] Ch. Borde, M. Ouhayoun, A. VanLerberghe, C.Salomon, S. Avrillier, C.Cantrell, and J.Borde,
Phys. Rev. Lett. 45, 14 (1980)

[30] K. Kim, W. Person, D. Seitz, and B. Krohn, J. Mol. Spectrosc. 76, 322(1979)

[31] W. G. Harter, Phys. RevA. 24, 192(1981)

[32] J. Bordé, Ch. J. Bordé: Chem. Phys.71,417(1982)

[33] R. J. Butcher, Ch. Chardonnet, Ch. Bordé: Phys. Rev.Lett.,70,2698(1993)

[34] H. W. Kroto, J. R. Heath, S. C. O'Brian, R. F. Curl, R. E. Smalley: Nature 318,162(1985)

[35] W. Kratschmer, W. D. Lamb, K. Fostiropolous, D. R. Huffman: Nature 347,354(1990)

[36] W. G. Harter, D. E. Weeks: Chem. Phys. Lett. 132,187(1986)
W. G. Harter, D. E. Weeks: J. Chem. Phys. 90,4727 (1989)

[37] D. E. Weeks, W. G. Harter: Chem. Phys. Lett.144,366 (1988)
D. E. Weeks, W. G. Harter: J. Chem. Phys. 90,4744 (1989)

[38] D. E. Weeks, W. G. Harter: Chem. Phys. Lett.176,209 (1991)
W. G. Harter, T. C. Reimer: J. Chem. Phys. 94, 5426 (1991)

[39] Tyle C. Reimer, W. G. Harter, J. Chem. Phys. 106, 1326 (1997)

[40] W. G. Harter, T. C. Reimer: Chem. Phys. Lett.194,230 (1992)
W. G. Harter, T. C. Reimer: *erratum* Chem. Phys. Lett.198,429 (1992)

[41] P. Bryan Changala, Marissa L. Weichman, Kevin F. Lee, Martin E. Fermann, Jun Ye
Science 363,49–54 (2019)

[42] B. Spaum, P.Changala, D.Patteraon, B.Bjork, O. Heckl, J. Doyle, Jun Ye; Nature 533, 517 (2016);
B. Bjork, T. Bui, O. Heckl, P.Changala, B. Spaum, P. Heu D. Follman, C. Deutsch, G. Cole M. Aspemeyer, M. Okumura, Jun Ye; Science 354, 444 (2016)

[43] W. R. Hamilton: Proc. R. Irish Acad. II,424(1844)

[44] W. R. Hamilton: Proc. R. Irish Acad. II,424(1844)

[45] W. R. Hamilton: Phi. Mag. 25,489(1844)

[46] W. Pauli: Z. Phys.37,601(1927)

[47] P. Jordan: Z. Phys.94,531(1935)

[48] J. Schwinger: Quantum Theory of Angular Momentum, ed. L.C.Biedenharn, H.vanDam (Academic, New York 1965) p. 229

[49] L. C. Biedenharn, J. D. Louck: Angular Momentum in Quantum Physics, Encyclopedia of Mathematics, Vol 8, ed. by G. C. Rota (Addison Wesley, Reading, Massachusetts 1981) p. 212

[50] I. I. Rabi, N. F. Ramsey, J. Schwinger: Rev. Mod. Phys.26, 167 (1954)

[51] R. P. Feynman, F. I. Vernon, R. W. Helwarth: J. Appl.Phys. 28,49(1957)

[52] W. G. Harter, N. dos Santos: Am. J. Phys.46, 251(1978)

[53] K. K. Lehmann: J. Chem. Phys. 79,1098(1983)

[54] W. G. Harter: J. Chem. Phys.85,5560(1986)

[55] Z. Li, L. Xiao, M. E. Kellman: J. Chem. Phys.92,2251(1990)

[56] W. G. Harter: Comp. Phys. Rep.8,319(1988),see pp. 378–85

[57] J. Ortigoso, I. Kleiner, J. T. Hougen: J. Chem. Phys.110,11688(1999)

[58] H. A. Jahn, E. Teller: Proc. R. Soc. London A161,220(1937)

[59] H. A. Jahn, E. Teller: Proc. R. Soc. London A164, 117(1938)

[60] Boudon, V.; Mitchell, J.; Domanskaya, A.; Maul, C.; Georges, R.; Benidar, A.; Harter, W.G. Mol. Phys. 58, 391–400(2012)

[61] M. Carlos and O. Gruson and C. Richard and V. Boudon and M. Rotger and X. Thomas and C. Maul and C. Sydow and A. Domanskaya and R. Georges and P. Soulard and O. Pirali and M. Goubet and P. Asselin and T.R. Huet, J. , Journal of Quantitative Spectroscopy and Radiative Transfer 201, 2273 (2017)

[62] W.G. Harter and J. C. Mitchell, Int. J. Mol. Phys. 14, 796 (2013)